Cell Metabolism

Article

Hepatic stellate cells regulate liver fatty acid utilization via plasmalemma vesicle-associated protein

Graphical abstract

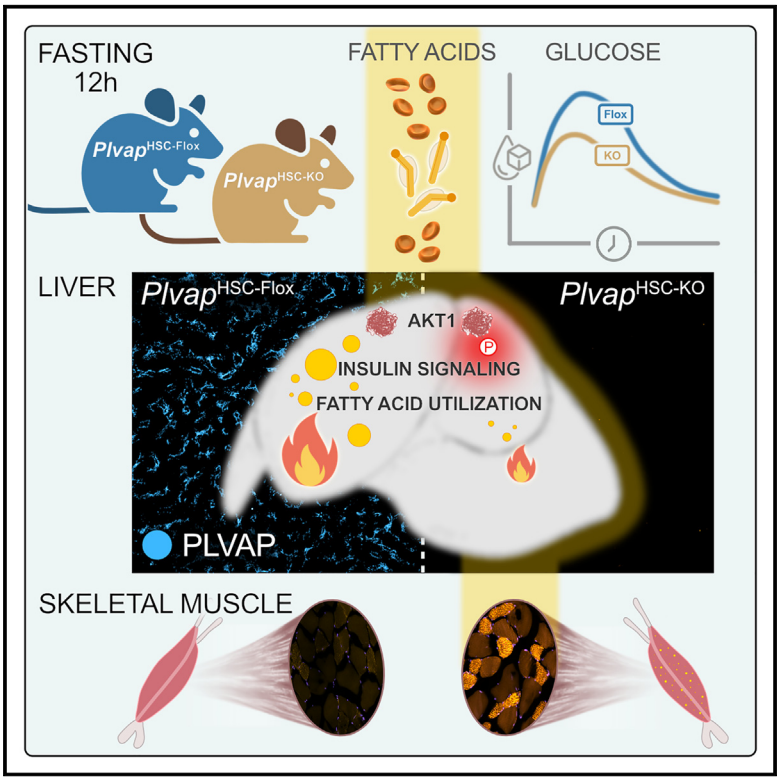

Highlights

- Plasmalemma vesicle-associated protein (PLVAP) has functions beyond the endothelium
- Hepatic stellate cell (HSC) PLVAP is required for fasting liver lipid utilization
- HSCs regulate fasting liver insulin signaling and energy substrate preference
- HSCs modulate whole-body lipid partitioning and glucose tolerance

Authors

Daniel Hansen, Jasmin E.R. Jensen, Christian A.T. Andersen, ..., Nils J. Færgeman, Marko Salmi, Kim Ravnskjaer

Correspondence

ravnskjaer@bmb.sdu.dk

In brief

Hansen et al. show that the hepatic stellate cell-expressed plasmalemma vesicle-associated protein is required for the normal switch from carbohydrate to lipid utilization during fasting. This reveals a novel layer of metabolic regulation imposed by perivascular cells of the liver, with possible implications for whole-body metabolism.

Hansen et al., 2025, Cell Metabolism *37*, 971–986
April 1, 2025
https://doi.org/10.1016/j.cmet.2025.01.022

CellPress

Cell Metabolism

CellPress
OPEN ACCESS

Article

Hepatic stellate cells regulate liver fatty acid utilization via plasmalemma vesicle-associated protein

Daniel Hansen,[1,2] Jasmin E.R. Jensen,[1] Christian A.T. Andersen,[1,2] Peter R. Jakobsgaard,[1,2] Jesper Havelund,[1] Line Lauritsen,[1] Samuel Mandacaru,[1] Majken Siersbaek,[1,2] Oliver L. Shackleton,[1] Hiroshi Inoue,[3] Jonathan R. Brewer,[1,2] Robert F. Schwabe,[4,5] Blagoy Blagoev,[1,2] Nils J. Færgeman,[1] Marko Salmi,[6,7,8] and Kim Ravnskjaer[1,2,9,*]

[1]Department of Biochemistry and Molecular Biology, University of Southern Denmark, 5230 Odense M, Denmark
[2]Center for Functional Genomics and Tissue Plasticity (ATLAS), University of Southern Denmark, 5230 Odense M, Denmark
[3]Metabolism and Nutrition Research Unit, Institute for Frontier Science Initiative, Kanazawa University, Kanazawa 920-8641, Ishikawa, Japan
[4]Department of Medicine, Columbia University, New York, NY 10032, USA
[5]Institute of Human Nutrition, Columbia University, New York, NY 10032, USA
[6]MediCity Research Laboratory, University of Turku, 20014 Turku, Finland
[7]Institute of Biomedicine, University of Turku, 20014 Turku, Finland
[8]InFLAMES Research Flagship Centre, University of Turku, 20014 Turku, Finland
[9]Lead contact
*Correspondence: ravnskjaer@bmb.sdu.dk
https://doi.org/10.1016/j.cmet.2025.01.022

SUMMARY

The liver is essential for normal fatty acid utilization during fasting. Circulating fatty acids are taken up by hepatocytes and esterified as triacylglycerols for either oxidative metabolization and ketogenesis or export. Whereas the regulation of fatty acid oxidation in hepatocytes is well understood, the uptake and retention of non-esterified fatty acids by hepatocytes is not. Here, we show that murine hepatic stellate cells (HSCs) and their abundantly expressed plasmalemma vesicle-associated protein (PLVAP) control hepatic substrate preference for fasting energy metabolism. HSC-specific ablation of PLVAP in mice elevated hepatic insulin signaling and improved glucose tolerance. Fasted HSC PLVAP knockout mice showed suppressed hepatic fatty acid esterification into di- and triacylglycerols, shifting fasting metabolism from fatty acid oxidation to reliance on carbohydrates. By super-resolution microscopy, we localized HSC PLVAP to caveolae residing along the sinusoidal lumen, supporting a role for HSCs and PLVAP-diaphragmed caveolae in normal fasting metabolism of the liver.

INTRODUCTION

Hepatocytes and non-parenchymal cells jointly maintain liver function, including metabolic and homeostatic processes. Liver sinusoidal endothelial cells (LSECs) and hepatic stellate cells (HSCs) are intimately associated along the hepatic microvasculature, the sinusoids. Confined to the space of Disse, HSCs envelop the sinusoids as pericytes and form extensive physical contacts with hepatocytes, LSECs, and Kupffer cells.[1–4] The discontinuous and fenestrated sinusoidal endothelium and sparse basal membrane expose hepatocytes and HSCs to plasma proteins, lipoproteins, and metabolites in circulation.[5] In the blood, non-esterified fatty acids (NEFAs) are associated with carrier proteins like albumin (Alb), ensuring NEFA solubility and facilitation of cellular uptake.[6] The liver is the nexus of fasting energy metabolism and its large capacity for fatty acid β-oxidation reflects the major catabolic pathway in hepatocytes during fasting. Yet, the regulation of NEFA uptake from the hepatic microcirculation and retention in hepatocytes remains incompletely understood.

Microvascular integrity of human and murine tissues, including the kidney, intestine, and lungs, relies on the membrane-associated glycoprotein plasmalemma vesicle-associated protein (PLVAP).[7–10] PLVAP forms spoke-like diaphragms across caveolae, fenestrae, and trans-endothelial channels in endothelia of highly vascularized tissues.[11–13] Caveolae are needed for normal lipid transport in white adipose tissue (WAT), in skeletal muscle, and in liver,[14–18] but mechanistic details are lacking. Mutations in the human *PLVAP* gene cause dyslipidemia, protein-losing enteropathy, and early death.[7,9,10] The importance of PLVAP for vascular integrity has further been studied in three independent murine *Plvap* knockout models showing strain-dependent phenotypic severity.[19–21] Also in mice, global loss of PLVAP increases embryonic lethality due to protein-losing enteropathy and edema. Studies have further concluded that whole-body *Plvap* ablation affected the liver vascular barrier, impairing both the egress of monocytes from the fetal liver during development and post-natal plasma lipoprotein clearance.[19,22,23] Importantly, post-natal liver sinusoidal fenestrae have no diaphragms, and hepatic PLVAP

itself is not required for LSEC fenestration.[19,24] Moreover, using single-cell transcriptomics, we previously demonstrated that HSCs, not LSECs, are the major PLVAP-expressing cells of adult mouse liver.[25] No function of PLVAP in non-endothelial cells of the liver or elsewhere has previously been reported.

Here, we describe the first cell-type-specific ablation of PLVAP in non-endothelial cells and reveal the first PLVAP functions outside the endothelium. We show that loss of PLVAP in HSCs, the liver sinusoidal pericytes, disrupts hepatic fasting metabolism, gene expression, and whole-body lipid partitioning. Our findings show that PLVAP and HSCs are critical for the uptake and retention of fatty acids from the liver sinusoid and their subsequent utilization by hepatocytes in fasting mice.

RESULTS

HSC *Plvap* knockout mice have histologically normal livers

To assess the hepatic expression of *Plvap*, we performed single-molecule RNA fluorescence *in situ* hybridization (smFISH) and immunofluorescence (IF) on adult mouse liver. Consistent with our prior findings,[25] but contrary to reports suggesting that PLVAP expression is endothelium specific,[24] sinusoidal *Plvap* mRNA was enriched in *Lrat*$^{+}$ HSCs (Figure 1A). PLVAP protein was co-expressed with the HSC marker Desmin[26] (Figure S1A). We detected only few *Plvap* transcripts overlapping with *Stab2*$^{+}$ LSECs (Figure S1B). Intrigued by PLVAP expression in pericytes, and set on determining the function of PLVAP in adult liver, we selectively disrupted the *Plvap* gene in HSCs by crossing *Plvap*$^{fl/fl}$ mice[21] with the *Lrat-Cre* strain.[27] *Lrat-Cre*$^{wt/tg}$-*Plvap*$^{fl/fl}$ mice (*Plvap*$^{HSC\text{-}KO}$) were born in the expected mendelian ratio and gained weight like littermate controls (*Plvap*$^{HSC\text{-}Flox}$) (Figure 1B). *Plvap*$^{HSC\text{-}KO}$ mice were fertile and appeared healthy, presenting none of the phenotypic traits of whole-body knockouts.[19–21]

We confirmed *Plvap* knockout at RNA and protein levels. *Plvap*$^{HSC\text{-}KO}$ mice invariably showed a 70% reduction in liver *Plvap* transcripts consistent with selective *Plvap* ablation in HSCs (Figure 1B). Using our *FLEx-TRAP* mCherry-RPL10A reporter strain,[28] we verified DESMIN^{+} HSC-specific *Lrat*-Cre activity (Figures S1C and S1D). Examination of hepatic PLVAP protein by IF confirmed near-complete loss of immunoreactivity to the monoclonal anti-PLVAP antibody (MECA-32) in *Plvap*$^{HSC\text{-}KO}$ livers (Figures 1B and 1C). The remaining PLVAP signal in *Plvap*$^{HSC\text{-}KO}$ livers localized mainly to venules, likely to vascular liver endothelial cells (LECs) (Figures 1C and S1E).

Sinusoidal localization of HSCs was not affected by PLVAP ablation. Using markers of HSCs, DESMIN (Figure 1C), and mesenchymal cells, PDGFRα/β (Figure S1F), we observed no morphological changes to HSC bodies nor to their cytoplasmic processes. Liver histology appeared normal in *Plvap*$^{HSC\text{-}KO}$ mice, as assessed by hematoxylin and eosin, picrosirius red staining for fibrillar collagen, and immunohistochemistry (IHC) for F4/80-positive macrophages representing mainly Kupffer cells (Figure 1D). Pre-prandial serum samples were optically identical between genotypes, showing no dyslipidemia, as was seen in global *Plvap* knockouts (Figure S1G). We next tested PLVAP expression in the small intestine, primarily affected in protein-losing enteropathy upon global loss of PLVAP.[7,19] In keeping with the healthy appearance of our *Plvap*$^{HSC\text{-}KO}$ mice, we readily detected PLVAP in *Plvap*$^{HSC\text{-}KO}$ duodenum (Figure 1C). Western blot analysis also confirmed loss of PLVAP protein in livers of *Plvap*$^{HSC\text{-}KO}$ mice but not in other PLVAP-rich tissues like the kidney and small intestine (Figure S1H). As whole-body *Plvap* knockouts suffer from vascular leakiness and plasma protein extravasation, we performed proteomics on serum from HSC-specific knockouts and measured total protein. We found no significant differences in abundance of serum albumin (ALB) nor major apolipoproteins and detected no difference in the total serum protein levels (Figures 1E and 1F). A slight but significant reduction in tissue factor (TF) levels and increases in the liver-expressed pregnancy-zone protein (PZP) and apolipoprotein M (APOM) were recorded in serum from knockout mice. Taken together, our data confirmed HSC-specific PLVAP deletion in *Plvap*$^{HSC\text{-}KO}$ mice, with no effects on liver histology nor total serum protein levels.

HSC PLVAP is required for the hepatic response to fasting

For a detailed view of the consequences of HSC-specific ablation of *Plvap* at the hepatic sinusoid, we sequenced RNA from liver tissue of 12-h-fasted *Plvap*$^{HSC\text{-}KO}$ and *Plvap*$^{HSC\text{-}Flox}$ mice (n = 5–6). This comparison identified 425 differentially expressed genes (DEGs) ($p_{adj} < 0.05$), many of which were associated with fatty acid utilization and its regulation (Figures 2A, S2A, and S2B). Ablation of *Plvap* led to a striking repression of peroxisome proliferator-activated receptor alpha (PPARα) target genes, including key genes in fatty acid handling and ketogenesis, such as *Acadl*, *Acat1*, *Acox1*, *Cidec*, *Cpt1a*, *Cyp4a12*, *Ehhadh*, and *Hmgcs2* (Figure 2A). These transcriptional changes would be expected to impair hepatic fatty acid storage and mitochondrial and peroxisomal β-oxidation, as well as ω-oxidation. PPARα is activated by fatty acids and their derivatives and is critical for the adaptive response to fasting.[29–31] The observed expression patterns overlapped substantially with those reported for *Ppara*$^{HEP\text{-}KO}$ and *Atgl*$^{WAT\text{-}KO}$ mice and could hence reflect the lack of endogenous PPARα ligands in *Plvap*$^{HSC\text{-}KO}$ livers (Figures S2C–S2E). The highly expressed plasma carriers *Alb* and afamin (*Afm*) were transcriptionally induced in *Plvap*$^{HSC\text{-}KO}$ livers (Figure 2A), but *Alb* gene induction did not translate into elevated serum ALB levels, as noted above (Figure 1E). We further recorded strong induction of the hepatokine *Gdf15*, also induced in other models of energy stress after compromised hepatic lipid oxidation[29,32] and recently found to increase systemic insulin sensitivity and skeletal muscle energy expenditure.[33,34] Conversely, neither core genes in lipogenesis (*Acaca* and *Fasn*) nor cholesterol synthesis (*Hmgcr*) were affected by *Plvap* ablation despite reduced expression of *Insig2* (Figure S2F) encoding a key regulator of the sterol regulatory element-binding proteins. Likewise, neither expression nor serum levels of the metabolic regulator fibroblast growth factor (FGF)21 were significantly different between fasting *Plvap*$^{HSC\text{-}KO}$ and controls (Figure S2G). Consistent with normal HSC appearance, we found only few HSC-enriched DEGs (Figure 2A), indicating that HSC-expressed PLVAP determines HSC-hepatocyte interactions rather than overall HSC function. HSC PLVAP ablation also modestly repressed the LEC genes *Kdr* and *Ptprb* and induced expression of the LSEC marker

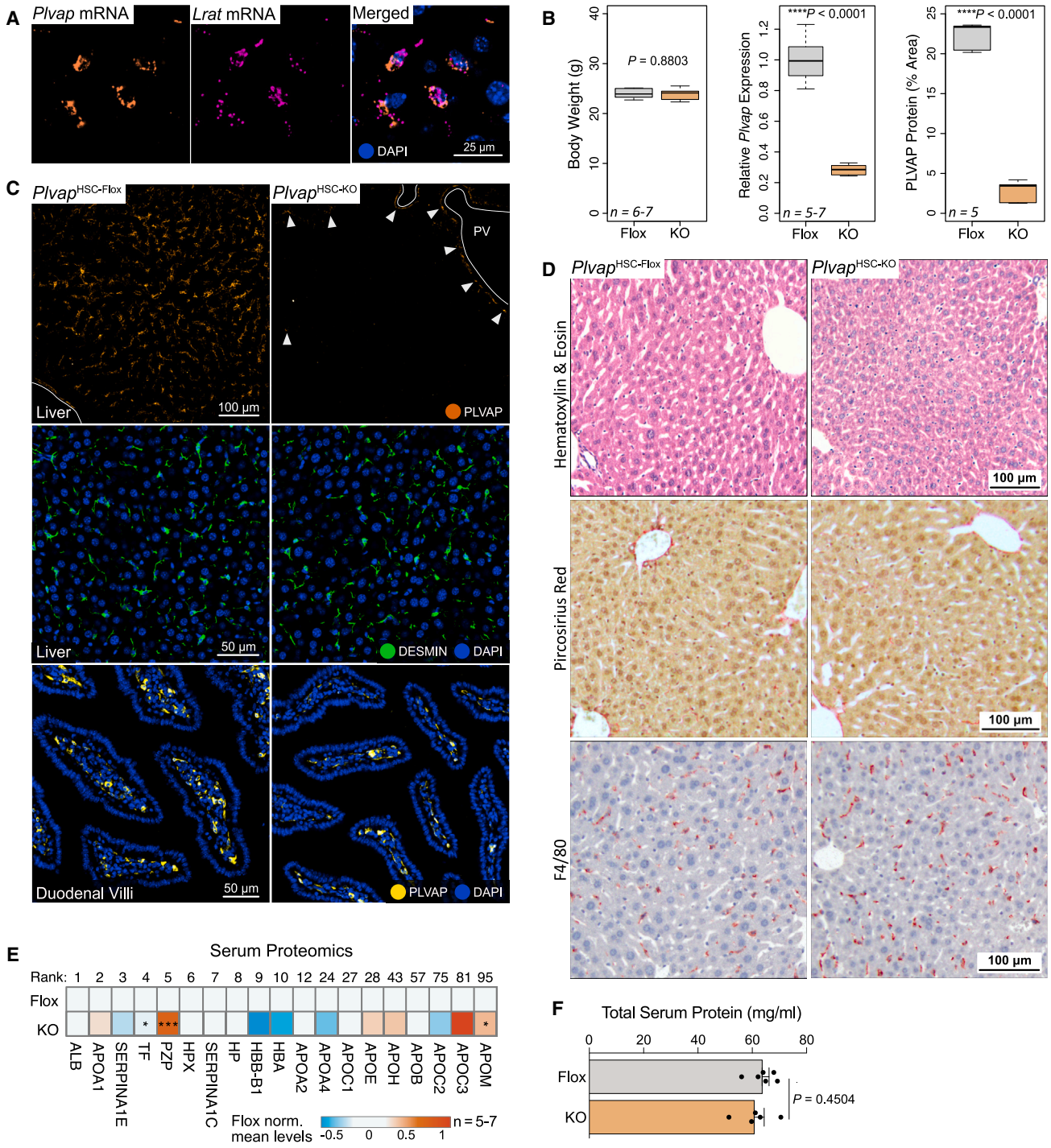

Figure 1. Hepatic stellate cell *Plvap* KO mice appear developmentally normal

(A) Single-molecule fluorescence *in situ* hybridization of *Plvap* and *Lrat* mRNA in murine liver.

(B) Body weight, relative *Plvap* mRNA, and PLVAP protein in *Plvap*$^{HSC\text{-}KO}$ (knockout [KO]) and littermate *Plvap*$^{HSC\text{-}Flox}$ (Flox) mice (n = 5–7, Welch's t-test). Boxplots show median, upper, and lower quartiles.

(C) Immunofluorescence of PLVAP and DESMIN in KO and Flox livers and duodenal villi. Venules and preserved PLVAP protein are indicated.

(D) Hematoxylin and eosin, picrosirius red, and F4/80-IHC staining of KO and Flox livers.

(E) Normalized abundances of ten most-abundant proteins and apolipoproteins detected by mass spectrometry in serum from KO and Flox mice (n = 5–7, $^{*}p_{adj} < 0.05$, $^{***}p_{adj} < 0.001$, Bonferroni-corrected t test).

(F) Total serum protein from KO and Flox mice (n = 5–7, Student's t-test). Data are represented as mean ± SEM.

See also Figure S1.

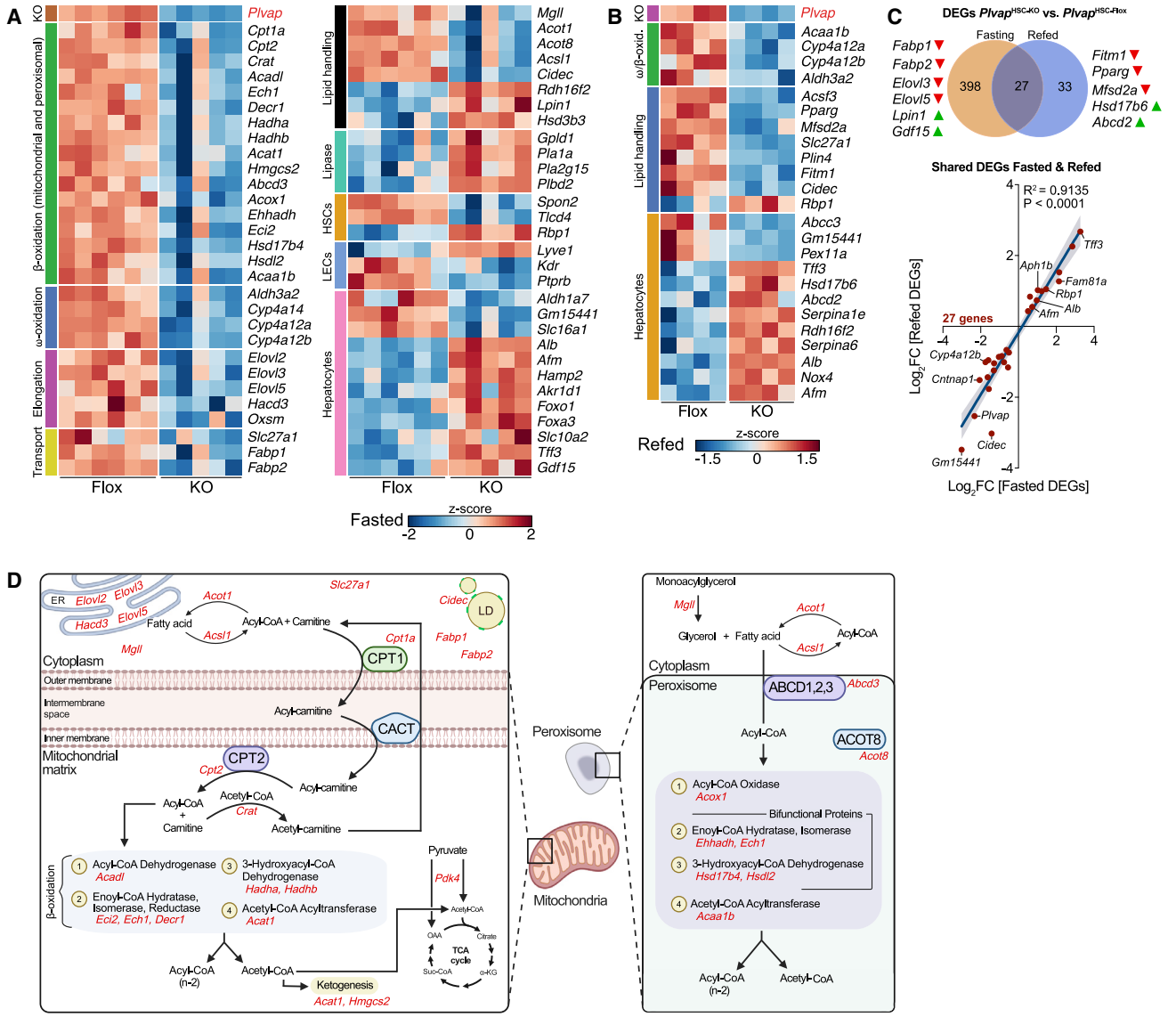

Figure 2. Hepatic stellate cell *Plvap* KO perturbs liver metabolic gene expression

(A) Normalized expression of selected, differentially expressed genes (DEGs) ($p_{adj} < 0.05$, $n = 5–6$, Wald test) comparing 12-h-fasted KO and Flox livers.

(B) Normalized expression of selected DEGs ($p_{adj} < 0.05$, $n = 4$, Wald test) comparing 2-h-refed KO and Flox livers.

(C) Top, Venn diagram of shared and condition-specific DEGs. Selected condition-specific DEGs and direction of change in KO shown. Bottom, scatterplot of shared DEGs in fasted and refed mice.

(D) Mitochondrial and peroxisomal fatty acid utilization pathways showing selected genes repressed in KO mice in red.

See also Figure S2.

Lyve1[35] (Figure 2A). The significance of these changes is currently unclear.

Having seen the profound impact of HSC PLVAP ablation on the hepatic adaptation to fasting, we gauged the importance of HSC PLVAP for the refeeding response. We sequenced RNA from livers of 12-h-fasted and 2-h-refed *Plvap*$^{HSC-KO}$ and *Plvap*$^{HSC-Flox}$ mice ($n = 4$) and found only 60 DEGs, 27 of which were implicated in lipid handling and showed similar changes in fasted animals (Figures 2B, 2C, and S2A). Curiously, in addition to repression of *Cidec*, refed *Plvap*$^{HSC-KO}$ livers had low expression of *Mfsd2a* and lipid-droplet-associated *Plin4* and *Fitm1* as well as the master regulator of lipid storage, PPARγ. Transcriptionally, fasted *Plvap*$^{HSC-KO}$ mice hence presented with altered lipid handling and metabolism as their main phenotype, which became less penetrant after refeeding. A schematic overview of affected lipid-metabolic pathways and genes is given in Figure 2D.

HSC PLVAP ablation zone specifically disrupts hepatic adaptation to fasting

Lipid profiles and lipid metabolic processes are zonated across the liver lobule.[36,37] To resolve the transcriptional changes in

CellPress
OPEN ACCESS

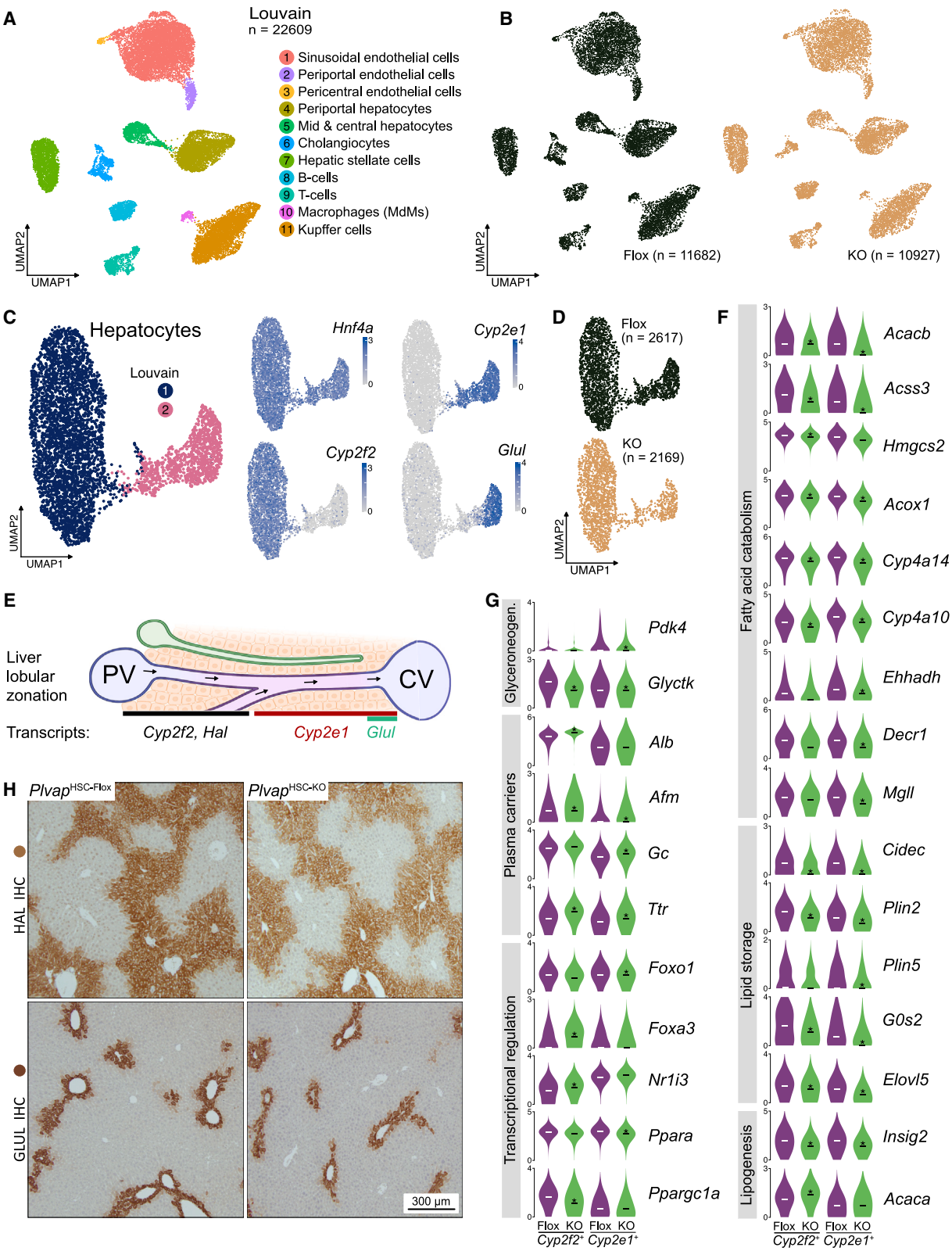

Figure 3. Hepatic stellate cell *Plvap* ablation zone specifically reshapes liver gene expression

(A) UMAP of 22,609 nuclei from KO and Flox livers showing Louvain clusters and cell-type annotations ($n = 3$).

(B) Nuclei stratified by genotype. Nucleus counts shown.

(legend continued on next page)

individual cell populations, we conducted single-nucleus RNA sequencing (snRNA-seq) of livers from fasted *Plvap*$^{HSC-KO}$ mice and littermate controls ($n = 3$). After quality control and integration, we visualized 22,609 high-quality nuclei by uniform manifold approximation and projection (UMAP) (Figures 3A and S3A). The nuclei clustered into 11 clusters representing major cell populations and each containing nuclei from all biological replicates across genotypes (Figures 3B and S3B–S3D). PLVAP transcripts were found in HSC nuclei, and HSC PLVAP ablation led to no changes in cell-type abundances (Figures S3E and S3F).

Subsetting of annotated nuclei allowed us to investigate subpopulations of interest, guided by our bulk RNA data. We subclustered the parenchymal population to obtain a detailed view on *Plvap* knockout-driven changes in hepatocytes. We resolved *Hnf4a*$^+$ hepatocytes and stratified these according to zonation markers *Cyp2f2*$^+$/*Sds*$^+$ (periportal), *Cyp2e1*$^+$ (midlobular/pericentral), and *Glul*$^+$ (pericentral)[38,39] (Figures 3C–3E). The three major zones were equally populated by nuclei of *Plvap*$^{HSC-KO}$ and littermate control livers. Comparing nuclei by genotype, we identified DEGs implicated in lipid metabolism and transport. Adding to our whole-liver gene expression analysis, genes involved in fatty acid utilization and ketogenesis, including *Acacb*, *Acox1*, *Acss3*, *Cyp4a10*, *Cyp4a14*, *Ehhadh*, *Hmgcs2*, and *Pdk4*, were repressed across pericentral and periportal hepatocytes (Figures 3F and 3G). Repression of *Pdk4* and *Glyctk*, encoding the pyruvate dehydrogenase kinase 4 and glycerate kinase, respectively, would suppress glyceroneogenesis and fatty acid esterification into triacylglycerols (TAGs). Similarly, genes directly implicated in TAG storage—*Cidec*, *Elovl5*, *G0s2*, *Plin2*, and *Plin5*—were repressed across all *Plvap*$^{HSC-KO}$ hepatocytes (Figure 3F). Also, zone-specific patterns were found. In contrast to bulk RNA levels, expression changes related to *de novo* lipogenesis were seen in periportal hepatocytes, pointing to increased fatty acid synthesis (Figure 3F). Likewise, induction of genes encoding the plasma carrier proteins *Alb*, *Afm*, and *Ttr* was strongest in periportal hepatocytes (Figure 3G) following known zonation patterns.[38] Hepatocyte-specific suppression of key metabolic regulators *Ppara*, *Ppargc1a*, and *Foxo1* further indicated perturbation of the gene regulatory networks underlying the hepatic fasting response. Notably, periportal expression of the hepatocyte lineage-defining factor *Foxa3* was induced (Figure 3G). At single-cell resolution, we hence confirmed the disruption of hepatocyte fatty acid handling programs upon HSC PLVAP ablation and elucidated zonated alterations in gene expression. We found no broader disruption of lobular zonation, which we confirmed by IHC against zonation markers: periportal HAL and pericentral GLUL proteins[38] (Figure 3H).

In keeping with the preserved liver histology, few changes were observed in HSC nuclei, showing that PLVAP, under the conditions studied, is not required for HSC identity or quiescence. A few genes associated with the quiescent HSC phenotype—*Nrxn3*, *Postn*, and *Gpc6*—were increased, whereas others—*Col14a1* and *Thsd7a*—were repressed (Figures S3G–S3I). Interestingly, *Alcam*, previously associated with HSC activation,[25] was repressed in *Plvap*$^{HSC-KO}$ HSCs despite being induced in whole liver. This discrepancy we ascribe to *Alcam*$^+$ cells not represented in our snRNA-seq dataset. Given the function of above HSC DEG products, changes may well have implications for HSC interactions with other hepatic cell populations. Similarly, we detected few changes in endothelial cells (Figures S3J–S3L) and macrophages (Figures S3M–S3O) following loss of HSC PLVAP, thus emphasizing the disruption of hepatocytes' adaptation to fasting as the major consequence of HSC PLVAP ablation.

HSC PLVAP is required for normal liver fatty acid utilization during fasting

To investigate whether the observed changes in hepatic gene expression translated into reduced fatty acid utilization, we fasted the mice in metabolic cages for indirect calorimetry (Figure 4A). Importantly, fasting *Plvap*$^{HSC-KO}$ mice indeed had an increased respiratory exchange ratio relative to littermate controls, consistent with a shift from fatty acids to carbohydrates as the dominant energy source. This switch led to reduced circulating β-hydroxybutyrate levels in fasting *Plvap*$^{HSC-KO}$ mice (Figure 4B). All mice displayed the typical diurnal pattern of nocturnal activity, with no difference in food consumption between genotypes. We detected no significant change in serum NEFA nor glycerol levels between *Plvap*$^{HSC-KO}$ mice and controls (Figures 4C and 4D) and no difference in WAT morphology (Figure S4A) to suggest defects in WAT lipolysis. Similarly, lean and fat mass distribution, as assessed by whole-body NMR, were not different between *Plvap*$^{HSC-KO}$ and control mice (Figure S4B). This supported the notion of defective hepatic fatty acid utilization and ketogenesis in *Plvap*$^{HSC-KO}$ mice during fasting despite what appeared as an intact adipose tissue lipolytic response.

Suppression of hepatic fatty acid utilization would aggravate fasting steatosis unless itself caused by reduced fatty acid availability blunting PPARα activation. To address the underlying cause, we imaged neutral lipids in *Plvap*$^{HSC-KO}$ and control livers. Strikingly, fasting littermate control mice had neutral lipid droplets distributed throughout the liver, whereas livers from fasted knockout mice were depleted of lipid droplets (Figure 4E). Accordingly, lipid droplet-associated perilipin-2 was largely absent in knockout livers (Figure S4C). Despite visible attenuation of hepatic steatosis in refed animals, the difference persisted after 2 h refeeding (Figure S4D). For a comprehensive examination of the fasting lipid content of *Plvap*$^{HSC-KO}$ livers, we applied mass spectrometry-based lipidomics. We found differences in the abundance of 93 lipid species ($p_{adj} < 0.05$), 52 of which were reduced with HSC PLVAP knockout and 41 elevated

(C) Subclustered hepatocyte nuclei and log1p expression of *Hnf4a* and zonation markers.
(D) Subsetted hepatocyte nuclei stratified by genotype. Nucleus counts shown.
(E) Depiction of zonated liver sinusoid with indication of zonation markers.
(F and G) Violin plots of $\log_{1p}$ expression of selected DEGs in hepatocytes stratified by genotype and *Cyp2f2*$^+$/*Cyp2e1*$^+$ expression-based zonation (* differentially expressed between KO and Flox; $p_{adj} < 0.05$, Wilcoxon rank-sum test). Medians shown.
(H) Representative immunohistochemistry against HAL and GLUL in KO and Flox livers.
See also Figure S3.

CellPress
OPEN ACCESS

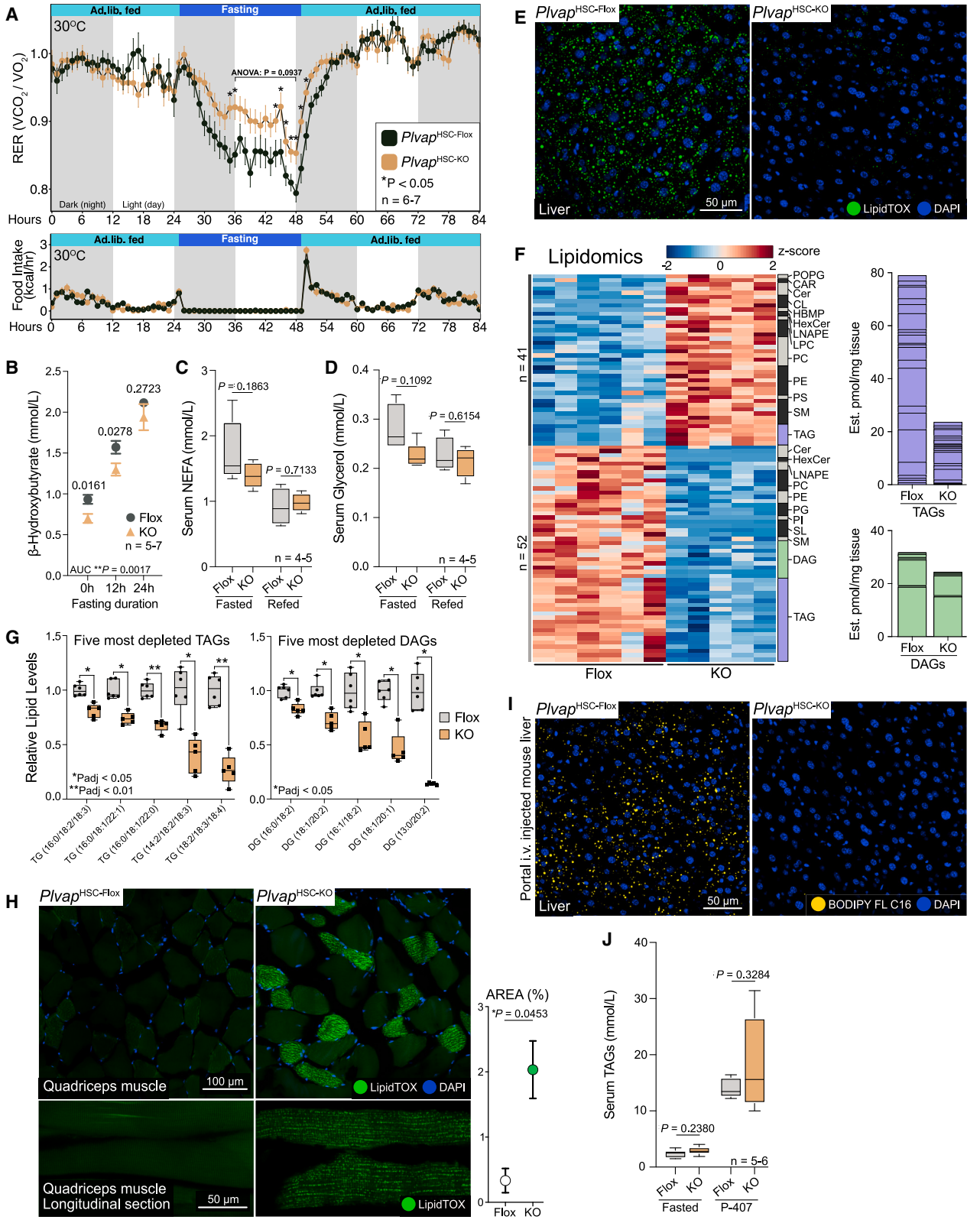

Figure 4. Hepatic stellate cell PLVAP is required for normal fatty acid utilization during fasting

(A) Respiratory exchange rate (RER, top) and food intake (bottom) of KO and Flox mice *ad libitum* fed or fasted at thermoneutrality (*$p < 0.05$, $n = 6–7$).

(B) Blood β-hydroxybutyrate from fed or 12-/24-h-fasted KO and Flox mice ($n = 5–7$, Welch's t-test).

(legend continued on next page)

(Figures 4F, S4E, and S4F). In line with depleted neutral lipid stores, we identified TAGs and diacylglycerols (DAGs) as the major lipid species reduced in the absence of HSC PLVAP. TAGs and DAGs constituted 60% of the depleted lipid species (Figures 4F and 4G), and absolute quantities of affected TAGs and DAGs were strongly reduced in *Plvap*$^{HSC-KO}$ livers (Figures 4F and S4G). Phospholipids and sphingomyelins were the prominent lipid species increased in knockout livers (Figure 4F), which also exhibited a notable rise in ether lipid contents (Figure S4G; data not shown). Acyl-carnitine levels were unaffected (data not shown).

Given comparable adipose tissues and circulating NEFA levels, defective uptake or esterification of NEFAs in livers of *Plvap*$^{HSC-KO}$ mice would be the likely explanation of their suppressed fatty acid utilization and storage during fasting. To test this hypothesis, we first examined extrahepatic tissues, as impaired hepatic fatty acid retention should increase deposition elsewhere. Importantly, we found strongly increased lipid accumulation in quadriceps femoris muscle fibers from knockout mice relative to controls (Figure 4H), while no differences were seen in heart or kidneys (Figure S4H; data not shown).

If the HSC-expressed PLVAP protein was indeed implicated in the hepatic uptake or esterification of NEFAs, retention of acutely administered exogenous fatty acids would also be compromised in *Plvap*$^{HSC-KO}$ mice. We therefore injected fluorescent BODIPY-C_{16} complexed to BSA into the portal vein of 12-h-fasted, anesthetized animals of both genotypes (n = 3–5) followed by a brief wash-out and immediate fixation. BODIPY-C_{16} is a fluorescent derivative of palmitate, thus representing the major fatty acid released by lipolysis from murine adipose tissue.[40] After a single pass through the liver, BODIPY-C_{16} was readily detected in lipid droplets of hepatocytes in control mice (Figure 4I). In a direct display of impaired lipid storage, we saw virtually no BODIPY-C_{16} in *Plvap*$^{HSC-KO}$ livers.

A fraction of NEFAs taken up by the liver are recirculated as TAGs in very-low-density lipoproteins (VLDL). We therefore tested for increased VLDL export in our knockout mice. After 12 h fasting, we gave the lipoprotein lipase (LPL)-inhibitor poloxamer-407[41,42] and fasted the mice for one additional hour before assessing chances in serum TAG levels. After acute LPL inhibition, both genotypes demonstrated significantly higher serum TAGs compared with vehicle controls, but we recorded no consistent difference between the genotypes (Figure 4J). Increased TAG export is hence unlikely to account for the HSC PLVAP knockout phenotype.

We next asked whether hepatic utilization of circulating NEFAs was also impaired in *ad libitum*-fed *Plvap*$^{HSC-KO}$ mice. To study fatty acid flux in non-fasted mice, we induced adipose tissue lipolysis by acute administration of the β3-adrenergic receptor agonist CL316,243 (CL).[43] CL significantly increased serum NEFA and glycerol to fasting levels 1 h after injection, indicative of stimulated lipolysis (Figures S4I and S4J). CL treatment also increased serum insulin (Figure S4K). Intriguingly, in contrast to the fasting situation, forced lipolysis and elevation of NEFA levels in the fed state led to hepatic lipid droplet formation indistinguishable between *Plvap*$^{HSC-KO}$ mice and littermate controls (Figure S4L). This showed that HSC PLVAP is not required for hepatocyte lipid droplet formation *per se* but rather hepatic retention of NEFAs during fasting.

In summary, *Plvap*$^{HSC-KO}$ mice exhibited a switch in liver fasting metabolism from utilization of fatty acid to carbohydrates and rerouting of circulating NEFAs to skeletal muscle.

Loss of HSC PLVAP enhances glucose tolerance and hepatic insulin signaling during fasting

The compromised lipid utilization in fasting *Plvap*$^{HSC-KO}$ mice prompted us to examine their use of carbohydrates. We therefore compared glucose tolerance between *Plvap*$^{HSC-KO}$ mice and littermate controls by intraperitoneal glucose tolerance testing (ipGTT). All animals had comparable glycemic levels at time zero after 12 h fasting (Figure 5A). Yet, consistent with a switch in preferred energy substrate, *Plvap*$^{HSC-KO}$ mice showed superior glucose clearance (Figure 5A). Also, hepatic glycogen content tended to be higher in *Plvap*$^{HSC-KO}$ mice without reaching significance (Figure 5B). These findings supported that fasting carbohydrate utilization was elevated in the absence of HSC PLVAP.

To explore the underlying cause, we measured circulating insulin levels and probed for AKT phosphorylation at Ser473 (pAKT) as a surrogate for insulin signaling. Whereas serum insulin levels were comparable between genotypes, liver pAKT was strongly elevated in fasting *Plvap*$^{HSC-KO}$ mice, approaching refed levels (Figures 5C–5E). Liver postprandial pAKT was similar between genotypes, as was skeletal muscle fasting pAKT (Figures 5D and S5A). An intraperitoneal insulin tolerance test further showed a tendency toward increased insulin sensitivity in the knockouts (Figure 5F). Unlike in control animals, *Plvap*$^{HSC-KO}$ blood glucose remained suppressed $\geq$120 min post insulin challenge.

Induction of PDK4 is pivotal for metabolic adaptation to fasting.[44] PDK4 inhibition of the pyruvate dehydrogenase complex drives pyruvate into the tricarboxylic acid cycle as oxaloacetate. This facilitates gluconeogenesis as well as hepatic glyceroneogenesis, the main source of glycerol 3-phosphate for DAGs and TAGs formation.[45,46] Importantly, hepatic PDK4 protein levels were strongly suppressed in fasted *Plvap*$^{HSC-KO}$ mice (Figures 5D and 5E), validating our snRNA-seq data.

Increased fasting pAKT and suppressed PDK4 levels indicate increased insulin receptor signaling. We therefore assessed the

(C and D) Serum non-esterified fatty acids (NEFAs) (C) and glycerol (D) from 12-h-fasted or 2-h-refed KO and Flox mice (n = 4–5, Welch's t-test).
(E) Neutral lipids in livers of 12-h-fasted KO and Flox mice (n = 5–6).
(F) Normalized abundancies of differentially abundant lipid species in livers from 12-h-fasted KO and Flox mice ($p_{adj} < 0.05$, n = 5–6, Student's t-test, Benjamini-Hochberg [BH] corrected). Right, estimated cumulative abundancies of affected tri- and diacylglycerol (TAG, DAG) species.
(G) Five most-depleted TAGs and DAGs (*$p_{adj} < 0.05$, **$p_{adj} < 0.01$, Student's t-test, BH corrected).
(H) Neutral lipids in skeletal muscle of 12-h-fasted KO and Flox mice (n = 3). Right, quantified lipid signal (Welch's t-test).
(I) Hepatic BODIPY-FL-C16 after portal vein-injection as BSA complexes in 12-h-fasted KO and Flox mice (n = 3–5).
(J) Serum TAGs from 12-h-fasted KO and Flox mice given the LPL inhibitor poloxamer-407 (P-407) or saline for 1 h prior to sacrifice (n = 5–6, Welch's t-test).
Boxplots show median, upper, and lower quartiles. Otherwise, data are represented as mean ± SEM.
See also Figure S4.

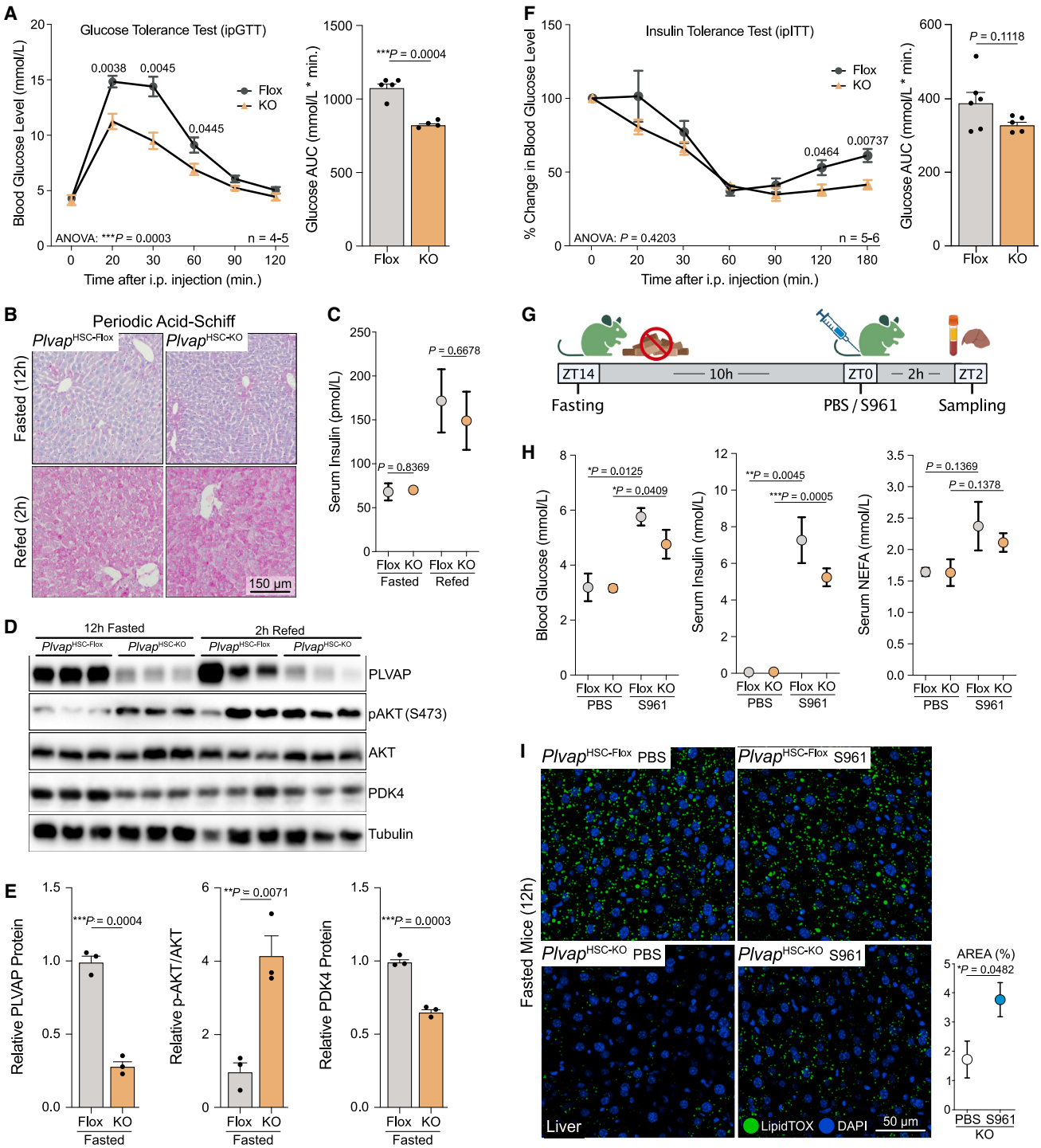

Figure 5. Hepatic stellate cell *Plvap* knockout improves glucose tolerance and fasting insulin receptor signaling

(A) Intraperitoneal (i.p.) glucose tolerance test of KO and Flox mice (*p* values from ANOVA and Student's t-tests shown). Right, area under the curve (AUC, *n* = 4–5, Welch's t-test).

(B and C) Periodic acid-Schiff-stained liver glycogen (B) and serum insulin (C) from 12-h-fasted or 2-h-refed KO and Flox mice (*n* = 3–5, Welch's t-test).

(D) PLVAP, pAKT, AKT, PDK4, and tubulin in liver lysates from 12-h-fasted or 2-h refed KO and Flox mice.

(E) Relative quantification of protein bands from fasted mice.

(F) I.p. insulin tolerance test of KO and Flox mice (*p*-values from ANOVA and Student's t-tests shown). Right, AUC (*n* = 5–6, Welch's t-test).

(G) Experimental design using the insulin receptor antagonist (S961) in fasted KO and Flox mice.

(legend continued on next page)

role of insulin action by using the selective insulin receptor antagonist S961[47] to acutely block insulin receptor signaling in our knockout animals. *Plvap*$^{HSC-KO}$ mice and littermate controls were fasted for 12 h and S961 or PBS was given subcutaneously 2 h before sacrifice (Figure 5G). S961 caused hyperglycemia and marked hyperinsulinemia yet suppressed hepatic AKT phosphorylation (Figures 5H and S5B). Serum NEFA and glycerol levels increased only slightly beyond normal fasting levels (Figures 5H and S5C). Strikingly, acute inhibition of the insulin receptor partially restored lipid droplet formation in *Plvap*$^{HSC-KO}$ hepatocytes, as assessed by LipidTOX staining, but had no effect on lipid levels in livers of control animals (Figure 5I). These findings strongly indicated that augmented hepatic insulin signaling of fasting HSC PLVAP knockout animals lies upstream of their lipid utilization phenotype.

An outstanding question to resolve was the phenotypic effect of HSC PLVAP ablation in the context of severe metabolic challenge. To test this, we fed *Plvap*$^{HSC-KO}$ and control mice either a Western diet with added fructose in the drinking water (WDF) or a 60% high-fat diet (HFD) for six weeks. Both diets caused weight gains and leveled liver AKT Ser473 phosphorylation between 12-h-fasted knockout and control mice (Figures S5D and S5E). Consistently, both diets reintroduced neutral lipids in the livers of fasting *Plvap*$^{HSC-KO}$ mice and offset genotype-driven differences in fasting liver gene expression (Figures S5F–S5I). A near-complete rescue of liver metabolic gene expression accompanied the more advanced steatosis in WDF-fed mice, implicating *de novo* lipogenesis in the reversal (Figure S5J). WDF + CCl_4-induced liver fibrosis was no different between genotypes (data not shown).

We have established that murine liver PLVAP expressed by HSCs is required for normal fatty acid utilization by hepatocytes during fasting. HSC PLVAP ablation augments liver insulin receptor signaling and shifts fasting metabolism toward use of carbohydrates. Perturbation of lipid homeostasis overrides the dependence on HSC PLVAP.

HSC PLVAP is associated with liver perisinusoidal caveolae

To elucidate the structural basis for perivascular PLVAP interactions with hepatocytes, we turned to super-resolution examination of knockout livers. We first performed scanning and transmission electron microscopy of *Plvap*$^{HSC-KO}$ and control livers to evaluate endothelial defenestration as the potential cause of altered lipid utilization. Sinusoidal fenestrations, distributed in characteristic sieve plates, were indistinguishable between control and *Plvap*$^{HSC-KO}$ livers (Figure 6A). Most LSEC fenestrations had diameters of 70–100 nm, regardless of PLVAP expression in HSCs (Figures 6A and S6A). PLVAP can form spoke-like fenestral or stomatal diaphragms spanning fenestra and caveola, respectively.[13,19] In agreement with previous reports,[24] neither genotype displayed fenestral diaphragms. To determine the subcellular location of PLVAP in HSCs, we applied super-resolution stimulated emission depletion (STED) microscopy. First, we visualized PLVAP together with genetically encoded mCherry-RPL10A in livers from *Lrat-Cre:FLEx-TRAP* mice.[28] Along sinusoids, PLVAP associated exclusively with mCherry-RPL10A$^+$ HSCs and formed punctate patterns peripherally along HSC bodies and processes (Figure 6B). Notably, we found PLVAP on both luminal and abluminal sides of the HSCs. We next immunolabeled PLVAP and caveolae proteins CAV1 and CAVIN1. Hepatic CAV1/CAVIN1 colocalization was also mostly seen along the hepatic sinusoids, denoting their presence in caveolae (Figure 6C). Similarly, resolving sinusoidal CAV1 with HSC-expressed PLVAP showed co-localization of the majority of both proteins near the sinusoid lumen, consistent with PLVAP-diaphragmed HSC caveolae (Figure 6C). Importantly, co-localization of CAV1 and CAVIN1 was unaffected by the absence of perisinusoidal PLVAP in *Plvap*$^{HSC-KO}$ livers (Figure 6D).

Caveolae are critical for membrane dynamics, mechanoprotection, and signaling[48,49] but also appear to be directly involved in metabolic regulation. Uptake of fatty acids is compromised in liver and adipose tissues of *Cav1* and *Cavin1* knockout mice, and *Cav1* is required for normal hepatic PPARα activity during fasting.[15,18,50–52] Having established a link between HSC PLVAP and liver caveolae, we performed bulk RNA-seq of livers from fasted, whole-body *Cav1*-deficient mice devoid of functional caveolae.[15] Reminiscent of *Plvap*$^{HSC-KO}$ livers, expression of *Ppara*, *Pparg*, *Cyp4a12a*, *Plin4*, *Lpin2*, and *Slc27a1* were found repressed and *Alb* increased in Cav1-null livers (Figures S6B and S6C). Likewise, visualization of neutral lipids in livers from fasted *Cav1*-deficient animals and age-matched controls showed defects in lipid accumulation (Figure S6D). Curiously, hepatic expression and perisinusoidal membrane localization of PLVAP was retained in *Cav1*-deficient animals (Figures S6E and S6F).

Taken together, our study shows that mouse liver PLVAP and HSCs govern fasting metabolism and partitioning of lipids. Loss of HSC PLVAP increases hepatic insulin signaling and shifts liver fasting metabolism from preferential utilization of fatty acids to carbohydrates. PLVAP modulation of hepatocyte metabolism likely involves HSC caveolae. This is the first account of PLVAP function in non-endothelial cells and the first demonstration of pericyte/HSC involvement in liver metabolic regulation.

DISCUSSION

Hepatic fatty acid metabolism is critical to uphold homeostasis during prolonged fasting. Although the regulation of fatty acid release from adipose tissue is well-described, less is known about the partitioning of circulating NEFAs between organs. Here, we report a novel role for HSCs in hepatic fatty acid utilization and the first function of PLVAP in non-endothelial cells. By cell-type-specific ablation in mice, we show that HSC-expressed PLVAP is essential for normal hepatocyte fatty acid retention and catabolism during fasting.

Past studies of whole-body *Plvap* knockout mice found severe disruptions of microvascular integrity, protein-losing enteropathy,

(H) Blood glucose, serum insulin, and NEFAs in 12-h-fasted KO and Flox mice given S961 or PBS for 2 h (n = 3, Welch's t-test).
(I) Neutral lipids in livers of 12-h-fasted KO and Flox mice given S961 or PBS 2 h prior to sacrifice (n = 3). Right, quantification of LipidTOX in livers of KO mice (Welch's t-test). Data are represented as mean ± SEM.
See also Figure S5.

CellPress
OPEN ACCESS

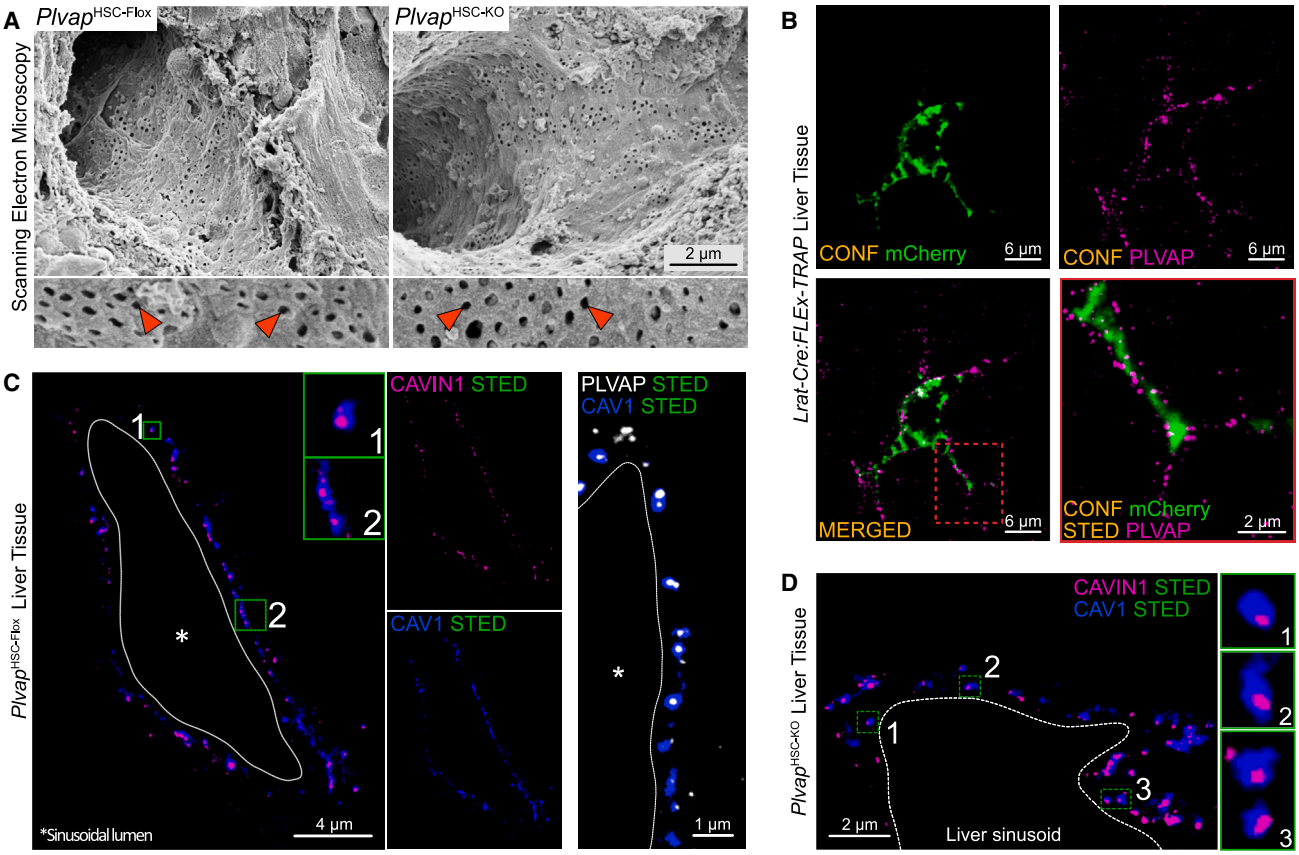

Figure 6. Hepatic stellate cell PLVAP localizes to perisinusoidal caveolae

(A) Scanning electron microscopy of sinusoidal lumens of KO and Flox livers (n = 3). Bottom, magnifications with arrows showing intact fenestrae.

(B) Combined confocal and stimulated emission depletion (STED) microscopy of PLVAP in an mCherry-RPL10A^{+} hepatic stellate cell in *Lrat-Cre:FLEx-TRAP* mouse liver.

(C) STED microscopy of hepatic CAVIN1, CAV1, and PLVAP proteins in Flox livers.

(D) STED microscopy of CAVIN1 and CAV1 protein in *Plvap* KO liver (n = 3). All images are representative for genotypes (n = 3).

See also Figure S6.

hypoalbuminemia, and hypertriglyceridemia.[19,20,23] Similar defects were observed in human infants with functional mutations in the *PLVAP* gene.[7,9,10] Phenotypic severity in human patients depends on the site of mutation, with less-severe phenotypes caused by PLVAP point mutants with retained capability to form fenestral diaphragms.[10] In mouse models, the phenotype is influenced by the genetic makeup, with whole-body PLVAP ablation on a pure C57BL/6 background being embryonically lethal.[8]

In our current study, *Plvap*$^{HSC-KO}$ mice deficient of PLVAP in HSCs retained PLVAP expression in the extra-hepatic tissues examined and showed normal serum protein content indicating normal vascular permeability. Body weight, body composition, and circulating lipid levels were not different from control animals suggesting normal adipose tissue function. Instead, fasted *Plvap*$^{HSC-KO}$ mice showed elevated hepatic insulin signaling accompanying a notable switch in energy substrate preference from fatty acids to continued carbohydrate utilization. Overall glucose tolerance was improved, and fasting carbohydrate utilization elevated. Meanwhile, fasted *Plvap*$^{HSC-KO}$ mice had defects in hepatocyte lipid storage and in fatty acid oxidation gene programs suggestive of compromised PPARα activation. Indeed, gene expression changes in *Plvap*$^{HSC-KO}$ livers overlapped with changes in *Atgl*$^{ADIPO-KO}$ and *Ppara*$^{HEP-KO}$ mice defective in adipose tissue lipolysis and hepatocyte fatty acid catabolism, respectively (Figures S2C–S2E).[29] In contrast to hepatocyte *Ppara* knockout, disruption of HSC PLVAP did not consistently affect the expression or circulating levels of FGF21, which is regarded as a systemic mediator of hepatic PPARα effects on energy expenditure.[53] Also, *Plvap*$^{HSC-KO}$ mice showed no defects in cold-induced thermogenesis (data not shown) clearly demonstrating locus-specific phenotypes of these otherwise comparable animal models.

TAGs accumulated in mixed-fiber quadriceps femoris muscles of fasting knockouts indicating redirection of NEFAs to skeletal muscle in the absence of liver sinusoidal PLVAP. Yet, improved glucose tolerance of *Plvap*$^{HSC-KO}$ mice suggests that the skeletal muscle lipid handling capacity met the increased availability and uptake. Curiously, both *Plvap*$^{HSC-KO}$ and *Ppara*$^{HEP-KO}$ livers showed elevated expression of *Gdf15*, which acts centrally through its receptor GFRAL to stimulate skeletal muscle fatty acid oxidation and energy expenditure.[34] Unlike fatty-acid-handling genes, liver expression of the plasma

NEFA carriers Alb and Afm were induced in *Plvap*$^{HSC-KO}$ mice. Alb synthesis is regulated by oncotic pressure[54] and stimulated in response to feeding by insulin and FGF15 (FGF19 in humans).[55,56] Chronic elevation of hepatocyte insulin receptor signaling may hence explain the increased Alb expression.

Murine HSC PLVAP co-localized with caveolar proteins CAV1 and CAVIN1, showing association with caveolae. Caveolae have previously been implicated in normal lipid handling by adipose tissue and the liver.[15,18] Whole-body knockout of *Cav1* resulted in a lipodystrophy phenotype with hypertriglyceridemia and compromised hepatic lipid utilization.[15,18,50] A general defect in fatty acid uptake and storage by adipose and liver tissues would bring about such phenotype. Hypertriglyceridemia in global *Plvap* knockout mice on a mixed background was previously ascribed to liver sinusoidal defenestration and impaired lipoprotein passage.[23] But, given the pronounced hepatic steatosis and inflammation in these mice, along with the loss of sinusoidal fenestrations, the primary defect is difficult to attribute solely to either liver or adipose tissue. In our present study, sinusoids of *Plvap*$^{HSC-KO}$ livers were devoid of PLVAP yet appeared normal with intact fenestrations. Similarly, in two global knockout models, no alterations in LSEC fenestrations were seen.[19,24] We therefore speculate that whole-body PLVAP ablation may cause adipose endothelium dysfunction and dyslipidemia[19,23] inducing hepatic inflammation and sinusoidal defenestration as secondary events.

Formation of hepatocyte lipid droplets during fasting likely serves to buffer incoming fatty acids. Structural studies have shown extensive contacts between lipid droplets, mitochondria, and the endoplasmic reticulum (ER) playing key roles in intracellular partitioning of fatty acids and esterification as TAGs.[57] Curiously, peri-droplet mitochondria support TAG formation, whereas highly oxidative mitochondria preferentially locate to the cytoplasm.[57] In keeping with zonated lipid metabolism, both mitochondria and peroxisomes further show functional specialization along the porto-central axis.[38,58–60] Many genes affected by HSC PLVAP ablation are related to peroxisomal function and enriched in the pericentral region where the mitochondrial oxidative capacity is lower.[59] During fasting, lipid droplets may here buffer fatty acid supply for peroxisomal oxidation, acetyl-coenzyme A (CoA) production, and pericentral ketogenesis. Aligning with our observations in *Plvap*$^{HSC-KO}$ mice, the loss of lipid droplets would disrupt this flow.

How HSC PLVAP regulates lipid droplet dynamics is currently not clear. In the healthy liver, NEFA-loaded albumin would freely traverse the fenestrated endothelium. HSC PLVAP and caveolae most likely orchestrate hepatic fatty acid utilization by modulating adjacent hepatocyte function rather than direct participation in fatty acid transport. Importantly, HSC PLVAP was required for hepatic lipid utilization specifically in healthy, fasted mice. Forced lipolysis in *ad libitum*-fed mice or prolonged high-calorie-diet feeding readily induced hepatocyte lipid droplets in both knockouts and littermate controls blunting differences between genotypes. We did not establish whether surging supplies to the liver of TAGs, NEFAs, or lipgenic substrates override normal regulation. If surging supplies to the liver of TAGs, NEFAs, or substrates for lipogenesis override regulation we did not establish. Yet, this may reflect how nutrient excess and metabolic dysfunction drive hepatic steatosis. Fasting *Plvap*$^{HSC-KO}$ mice showed sustained hepatic AKT phosphorylation, improved glucose tolerance, and a marked tendency for improved insulin sensitivity. Notably, acute administration of the selective insulin receptor antagonist S961 reverted the phenotype, leading to the reappearance of lipid droplets. We hence propose that caveolar PLVAP shape HSC-hepatocyte crosstalk, modulating hepatocyte insulin signaling during fasting. Consistently, selective disruption of hepatocyte insulin signaling in liver insulin-receptor knockout (LIRKO) mice increased fasting liver TAG accumulation.[61] Insulin suppression of TAG accumulation in the healthy liver contrasts its antilipolytic effect on adipose tissue, but, together, they could explain the loss of hepatic lipid droplets upon refeeding despite insulin inhibition of both fatty acid oxidation[62] and VLDL secretion.[63,64]

Caveolae act as hubs for compartmentalized cell signaling.[48,49,65] Given the phenotype of our *Plvap*$^{HSC-KO}$ mice, we speculate that PLVAP could control either caveolae internalization or clustering of caveolae-associated cell surface proteins implicated in signaling in the space of Disse. Caveolar proteins CAV1, CAVIN1, and EHD2 were previously found to cell-autonomously modulate insulin signaling.[16,66,67] Whether similar mechanisms apply to paracrine regulation of insulin signaling awaits further study. Nevertheless, contrasts are striking between HSC PLVAP ablation, loss of hepatic triglycerides, increased insulin signaling, and glucose uptake and the enhanced lipid droplet formation, suppressed insulin signaling, and glucose uptake in *Ehd2* knockout animals.[14,67] EHD2 oligomerizes around the neck of caveolae and stabilizes them at the plasma membrane.[14]

Molecular crosstalk between the sinusoidal niche and hepatocytes is largely unexplored, and future studies will clarify the molecular nature of the PLVAP-dependent HSC-hepatocyte crosstalk in the fasting liver. Vascular endothelial function is linked to insulin action,[68] and our current study may extend this connection to pericytes. Indeed, a recent genome-wide association study found single-nucleotide variants enriched in pericyte open chromatin associated with traits of the metabolic syndrome and type 2 diabetes.[69] Whether this association goes beyond regulation of blood flow, and whether PLVAP is expressed by pericytes rather than the endothelium in other tissues, merits further investigation.

This is the first functional study of PLVAP in non-endothelial cells and the first study to show liver sinusoidal pericyte involvement in metabolic regulation. Our findings will have implications for the understanding of insulin action and energy substrate preference in both healthy tissues and after injury, where PLVAP is commonly induced in the adjacent endothelia.

Limitations of the study

We used the *Lrat-Cre* driver for the first conditional ablation of PLVAP outside the endothelium. The *Lrat-Cre* driver is ideal for HSC-specific knockout in the liver but may be active in other adult tissues and during development. Non-HSC Cre-activity in *Plvap*-expressing cell types could affect our study. Also, we currently do not know when during development *Plvap* is first expressed in HSCs and would need an inducible system to discern the effects of PLVAP depletion on metabolism at the time of study from earlier impact on homeostatic setpoints. Additional studies are needed to establish whether the HSC PLVAP effects on hepatocyte function are direct or in part conveyed by the other sinusoidal cell types, LSECs or KCs. All mice in this study were male mice.

RESOURCE AVAILABILITY

Lead contact

Further information and requests should be directed to and will be fulfilled by the lead contact, Kim Ravnskjaer (ravnskjaer@bmb.sdu.dk).

Materials availability

This study did not generate new, unique reagents.

Data and code availability

Values used for graphs and full lists of differentially abundant transcripts and lipids are available in the Data S1- *source data* table. Raw and processed bulk RNA-seq and snRNA-seq data files have been deposited in NCBI's Gene Expression Omnibus (accession no. GEO: GSE246088). Proteomics data have been deposited to the ProteomeXchange Consortium via the PRIDE partner repository (accession no: PRIDE: PXD046745). This article does not report original code. Data analysis is described in the STAR Methods section of this article and additional information required to reanalyze the data is available from the lead contact upon request.

ACKNOWLEDGMENTS

We thank Maibrith Wishoff and Dr. Ronni Nielsen for technical assistance. We further acknowledge the Laboratory of Electron Microscopy, Institute of Biomedicine, and the Materials Research Infrastructure (MARI) at the Department of Physics and Astronomy, University of Turku, for access to TEM and SEM facilities and technical help. We thank Professor James G. Granneman, Wayne State University, MI, and Reader Carsten G. Hansen, University of Edinburgh, UK, for valuable discussions. Elements of the graphical abstract and Figure 5 were created using Biorender.com.

This work was supported by the Danish National Research Foundation (grant DNRF141) to the Center for Functional Genomics and Tissue Plasticity, the Independent Research Fund Denmark grant number 1030-00390B, and a fellowship (D.H.) from the Danish Diabetes Academy, which was funded by the Novo Nordisk Foundation (NNF), grant number NNF17SA0031406. Proteomics work was supported by the NNF (NNF18OC0052768 and the INTEGRA research infrastructure). Bioimaging was mainly performed at DaMBIC, a bioimaging research core facility at SDU, established by a grant from The Danish Agency for Science, Technology and Innovation and intramural funding.

AUTHOR CONTRIBUTIONS

D.H. and K.R. conceptualized the study. D.H. handled mouse work and genetic screening. D.H. and K.R. developed the study methodology. D.H., J.E.R.J., O.L.S., J.H., L.L., S.M., and M.S. conducted the formal investigation. D.H., C.A.T.A., P.R.J., and K.R. performed the NGS data analysis. D.H. and J.H. performed lipidomics. S.M. performed proteomics. K.R., M.S., N.J.F., B.B., J.R.B., H.I., and R.F.S. provided resources for the study. D.H. and K.R. prepared and wrote the manuscript. K.R. supervised and coordinated the study.

DECLARATION OF INTERESTS

The authors declare no competing interests.

STAR★METHODS

Detailed methods are provided in the online version of this paper and include the following:

SUPPLEMENTAL INFORMATION

Supplemental information can be found online at https://doi.org/10.1016/j.cmet.2025.01.022.

Received: December 12, 2023
Revised: November 26, 2024
Accepted: January 24, 2025
Published: March 3, 2025

REFERENCES

1. Bonnardel, J., T'Jonck, W., Gaublomme, D., Browaeys, R., Scott, C.L., Martens, L., Vanneste, B., De Prijck, S., Nedospasov, S.A., Kremer, A., et al. (2019). Stellate Cells, Hepatocytes, and Endothelial Cells Imprint the Kupffer Cell Identity on Monocytes Colonizing the Liver Macrophage Niche. Immunity *51*, 638–654.e9. https://doi.org/10.1016/j.immuni.2019.08.017.
2. Wake, K. (2006). Hepatic stellate cells: Three-dimensional structure, localization, heterogeneity and development. Proc. Jpn. Acad. Ser. B Phys. Biol. Sci. *82*, 155–164. https://doi.org/10.2183/pjab.82.155.
3. Wake, K., and Sato, T. (2015). "The sinusoid" in the liver: lessons learned from the original definition by Charles Sedgwick Minot (1900). Anat. Rec. (Hoboken) *298*, 2071–2080. https://doi.org/10.1002/ar.23263.
4. Wisse, E., De Zanger, R.B., Charels, K., Van Der Smissen, P., and McCuskey, R.S. (1985). The liver sieve: considerations concerning the structure and function of endothelial fenestrae, the sinusoidal wall and the space of Disse. Hepatology *5*, 683–692. https://doi.org/10.1002/hep.1840050427.
5. Poisson, J., Lemoinne, S., Boulanger, C., Durand, F., Moreau, R., Valla, D., and Rautou, P.E. (2017). Liver sinusoidal endothelial cells: Physiology and role in liver diseases. J. Hepatol. *66*, 212–227. https://doi.org/10.1016/j.jhep.2016.07.009.
6. van der Vusse, G.J. (2009). Albumin as fatty acid transporter. Drug Metab. Pharmacokinet. *24*, 300–307. https://doi.org/10.2133/dmpk.24.300.
7. Elkadri, A., Thoeni, C., Deharvengt, S.J., Murchie, R., Guo, C., Stavropoulos, J.D., Marshall, C.R., Wales, P., Bandsma, R., Cutz, E., et al. (2015). Mutations in Plasmalemma Vesicle Associated Protein Result in Sieving Protein-Losing Enteropathy Characterized by Hypoproteinemia, Hypoalbuminemia, and Hypertriglyceridemia. Cell. Mol. Gastroenterol. Hepatol. *1*, 381–394.e7. https://doi.org/10.1016/j.jcmgh.2015.05.001.
8. Bosma, E.K., van Noorden, C.J.F., Schlingemann, R.O., and Klaassen, I. (2018). The role of plasmalemma vesicle-associated protein in pathological breakdown of blood-brain and blood-retinal barriers: potential novel

therapeutic target for cerebral edema and diabetic macular edema. Fluids Barriers CNS *15*, 24. https://doi.org/10.1186/s12987-018-0109-2.

9. Broekaert, I.J., Becker, K., Gottschalk, I., Körber, F., Dötsch, J., Thiele, H., Altmüller, J., Nürnberg, P., Hünseler, C., and Cirak, S. (2018). Mutations in plasmalemma vesicle-associated protein cause severe syndromic protein-losing enteropathy. J. Med. Genet. *55*, 637–640. https://doi.org/10.1136/jmedgenet-2018-105262.
10. Kurolap, A., Eshach-Adiv, O., Gonzaga-Jauregui, C., Dolnikov, K., Mory, A., Paperna, T., Hershkovitz, T., Overton, J.D., Kaplan, M., Glaser, F., et al. (2018). Establishing the role of PLVAP in protein-losing enteropathy: a homozygous missense variant leads to an attenuated phenotype. J. Med. Genet. *55*, 779–784. https://doi.org/10.1136/jmedgenet-2018-105299.
11. Stan, R.V., Kubitza, M., and Palade, G.E. (1999). PV-1 is a component of the fenestral and stomatal diaphragms in fenestrated endothelia. Proc. Natl. Acad. Sci. USA *96*, 13203–13207. https://doi.org/10.1073/pnas.96.23.13203.
12. Stan, R.V., Ghitescu, L., Jacobson, B.S., and Palade, G.E. (1999). Isolation, cloning, and localization of rat PV-1, a novel endothelial caveolar protein. J. Cell Biol. *145*, 1189–1198. https://doi.org/10.1083/jcb.145.6.1189.
13. Tkachenko, E., Tse, D., Sideleva, O., Deharvengt, S.J., Luciano, M.R., Xu, Y., McGarry, C.L., Chidlow, J., Pilch, P.F., Sessa, W.C., et al. (2012). Caveolae, fenestrae and transendothelial channels retain PV1 on the surface of endothelial cells. PLoS One *7*, e32655. https://doi.org/10.1371/journal.pone.0032655.
14. Matthaeus, C., Lahmann, I., Kunz, S., Jonas, W., Melo, A.A., Lehmann, M., Larsson, E., Lundmark, R., Kern, M., Blüher, M., et al. (2020). EHD2-mediated restriction of caveolar dynamics regulates cellular fatty acid uptake. Proc. Natl. Acad. Sci. USA *117*, 7471–7481. https://doi.org/10.1073/pnas.1918415117.
15. Razani, B., Combs, T.P., Wang, X.B., Frank, P.G., Park, D.S., Russell, R.G., Li, M., Tang, B., Jelicks, L.A., Scherer, P.E., et al. (2002). Caveolin-1-deficient mice are lean, resistant to diet-induced obesity, and show hypertriglyceridemia with adipocyte abnormalities. J. Biol. Chem. *277*, 8635–8647. https://doi.org/10.1074/jbc.M110970200.
16. Liu, L., Brown, D., McKee, M., Lebrasseur, N.K., Yang, D., Albrecht, K.H., Ravid, K., and Pilch, P.F. (2008). Deletion of Cavin/PTRF causes global loss of caveolae, dyslipidemia, and glucose intolerance. Cell Metab. *8*, 310–317. https://doi.org/10.1016/j.cmet.2008.07.008.
17. Kim, C.A., Delépine, M., Boutet, E., El Mourabit, H., Le Lay, S., Meier, M., Nemani, M., Bridel, E., Leite, C.C., Bertola, D.R., et al. (2008). Association of a homozygous nonsense caveolin-1 mutation with Berardinelli-Seip congenital lipodystrophy. J. Clin. Endocrinol. Metab. *93*, 1129–1134. https://doi.org/10.1210/jc.2007-1328.
18. Fernández-Rojo, M.A., Gongora, M., Fitzsimmons, R.L., Martel, N., Martin, S.D., Nixon, S.J., Brooks, A.J., Ikonomopoulou, M.P., Martin, S., Lo, H.P., et al. (2013). Caveolin-1 is necessary for hepatic oxidative lipid metabolism: evidence for crosstalk between caveolin-1 and bile acid signaling. Cell Rep. *4*, 238–247. https://doi.org/10.1016/j.celrep.2013.06.017.
19. Stan, R.V., Tse, D., Deharvengt, S.J., Smits, N.C., Xu, Y., Luciano, M.R., McGarry, C.L., Buitendijk, M., Nemani, K.V., Elgueta, R., et al. (2012). The diaphragms of fenestrated endothelia: gatekeepers of vascular permeability and blood composition. Dev. Cell *23*, 1203–1218. https://doi.org/10.1016/j.devcel.2012.11.003.
20. Herrnberger, L., Seitz, R., Kuespert, S., Bösl, M.R., Fuchshofer, R., and Tamm, E.R. (2012). Lack of endothelial diaphragms in fenestrae and caveolae of mutant Plvap-deficient mice. Histochem. Cell Biol. *138*, 709–724. https://doi.org/10.1007/s00418-012-0987-3.
21. Rantakari, P., Auvinen, K., Jäppinen, N., Kapraali, M., Valtonen, J., Karikoski, M., Gerke, H., Iftakhar-E-Khuda, I., Keuschnigg, J., Umemoto, E., et al. (2015). The endothelial protein PLVAP in lymphatics controls the entry of lymphocytes and antigens into lymph nodes. Nat. Immunol. *16*, 386–396. https://doi.org/10.1038/ni.3101.
22. Rantakari, P., Jäppinen, N., Lokka, E., Mokkala, E., Gerke, H., Peuhu, E., Ivaska, J., Elima, K., Auvinen, K., and Salmi, M. (2016). Fetal liver endothelium regulates the seeding of tissue-resident macrophages. Nature *538*, 392–396. https://doi.org/10.1038/nature19814.
23. Herrnberger, L., Hennig, R., Kremer, W., Hellerbrand, C., Goepferich, A., Kalbitzer, H.R., and Tamm, E.R. (2014). Formation of fenestrae in murine liver sinusoids depends on plasmalemma vesicle-associated protein and is required for lipoprotein passage. PLoS One *9*, e115005. https://doi.org/10.1371/journal.pone.0115005.
24. Auvinen, K., Lokka, E., Mokkala, E., Jäppinen, N., Tyystjärvi, S., Saine, H., Peurla, M., Shetty, S., Elima, K., Rantakari, P., et al. (2019). Fenestral diaphragms and PLVAP associations in liver sinusoidal endothelial cells are developmentally regulated. Sci. Rep. *9*, 15698. https://doi.org/10.1038/s41598-019-52068-x.
25. Terkelsen, M.K., Bendixen, S.M., Hansen, D., Scott, E.A.H., Moeller, A.F., Nielsen, R., Mandrup, S., Schlosser, A., Andersen, T.L., Sorensen, G.L., et al. (2020). Transcriptional Dynamics of Hepatic Sinusoid-Associated Cells After Liver Injury. Hepatology *72*, 2119–2133. https://doi.org/10.1002/hep.31215.
26. Yokoi, Y., Namihisa, T., Kuroda, H., Komatsu, I., Miyazaki, A., Watanabe, S., and Usui, K. (1984). Immunocytochemical detection of desmin in fat-storing cells (Ito cells). Hepatology *4*, 709–714. https://doi.org/10.1002/hep.1840040425.
27. Mederacke, I., Hsu, C.C., Troeger, J.S., Huebener, P., Mu, X., Dapito, D.H., Pradere, J.P., and Schwabe, R.F. (2013). Fate tracing reveals hepatic stellate cells as dominant contributors to liver fibrosis independent of its aetiology. Nat. Commun. *4*, 2823. https://doi.org/10.1038/ncomms3823.
28. Bendixen, S.M., Jakobsgaard, P.R., Hansen, D., Hejn, K.H., Terkelsen, M.K., Bjerre, F.A., Thulesen, A.P., Eriksen, N.G., Hallenborg, P., Geng, Y., et al. (2024). Single cell-resolved study of advanced murine MASH reveals a homeostatic pericyte signaling module. J. Hepatol. *80*, 467–481. https://doi.org/10.1016/j.jhep.2023.11.001.
29. Fougerat, A., Schoiswohl, G., Polizzi, A., Régnier, M., Wagner, C., Smati, S., Fougeray, T., Lippi, Y., Lasserre, F., Raho, I., et al. (2022). ATGL-dependent white adipose tissue lipolysis controls hepatocyte PPARalpha activity. Cell Rep. *39*, 110910. https://doi.org/10.1016/j.celrep.2022.110910.
30. Régnier, M., Polizzi, A., Lippi, Y., Fouché, E., Michel, G., Lukowicz, C., Smati, S., Marrot, A., Lasserre, F., Naylies, C., et al. (2018). Insights into the role of hepatocyte PPARalpha activity in response to fasting. Mol. Cell. Endocrinol. *471*, 75–88. https://doi.org/10.1016/j.mce.2017.07.035.
31. Desvergne, B., and Wahli, W. (1999). Peroxisome proliferator-activated receptors: nuclear control of metabolism. Endocr. Rev. *20*, 649–688. https://doi.org/10.1210/edrv.20.5.0380.
32. Lee, J., Choi, J., Scafidi, S., and Wolfgang, M.J. (2016). Hepatic Fatty Acid Oxidation Restrains Systemic Catabolism during Starvation. Cell Rep. *16*, 201–212. https://doi.org/10.1016/j.celrep.2016.05.062.
33. Sjøberg, K.A., Sigvardsen, C.M., Alvarado-Diaz, A., Andersen, N.R., Larance, M., Seeley, R.J., Schjerling, P., Knudsen, J.G., Katzilieris-Petras, G., Clemmensen, C., et al. (2023). GDF15 increases insulin action in the liver and adipose tissue via a beta-adrenergic receptor-mediated mechanism. Cell Metab. *35*, 1327–1340.e5. https://doi.org/10.1016/j.cmet.2023.06.016.
34. Wang, D., Townsend, L.K., DesOrmeaux, G.J., Frangos, S.M., Batchuluun, B., Dumont, L., Kuhre, R.E., Ahmadi, E., Hu, S., Rebalka, I.A., et al. (2023). GDF15 promotes weight loss by enhancing energy expenditure in muscle. Nature *619*, 143–150. https://doi.org/10.1038/s41586-023-06249-4.
35. Halpern, K.B., Shenhav, R., Massalha, H., Toth, B., Egozi, A., Massasa, E.E., Medgalia, C., David, E., Giladi, A., Moor, A.E., et al. (2018). Paired-cell sequencing enables spatial gene expression mapping of liver endothelial cells. Nat. Biotechnol. *36*, 962–970. https://doi.org/10.1038/nbt.4231.
36. Seubnooch, P., Montani, M., Tsouka, S., Claude, E., Rafiqi, U., Perren, A., Dufour, J.F., and Masoodi, M. (2023). Characterisation of hepatic lipid signature distributed across the liver zonation using mass spectrometry imaging. JHEP Rep. *5*, 100725. https://doi.org/10.1016/j.jhepr.2023.100725.
37. Hall, Z., Bond, N.J., Ashmore, T., Sanders, F., Ament, Z., Wang, X., Murray, A.J., Bellafante, E., Virtue, S., Vidal-Puig, A., et al. (2017). Lipid

zonation and phospholipid remodeling in nonalcoholic fatty liver disease. Hepatology *65*, 1165–1180. https://doi.org/10.1002/hep.28953.

38. Halpern, K.B., Shenhav, R., Matcovitch-Natan, O., Toth, B., Lemze, D., Golan, M., Massasa, E.E., Baydatch, S., Landen, S., Moor, A.E., et al. (2017). Single-cell spatial reconstruction reveals global division of labour in the mammalian liver. Nature *542*, 352–356. https://doi.org/10.1038/nature21065.
39. Ma, R., Martínez-Ramírez, A.S., Borders, T.L., Gao, F., and Sosa-Pineda, B. (2020). Metabolic and non-metabolic liver zonation is established non-synchronously and requires sinusoidal Wnts. eLife *9*, e46206. https://doi.org/10.7554/eLife.46206.
40. Zhang, S., Williams, K.J., Verlande-Ferrero, A., Chan, A.P., Su, G.B., Kershaw, E.E., Cox, J.E., Maschek, J.A., Shapira, S.N., Christofk, H.R., et al. (2024). Acute activation of adipocyte lipolysis reveals dynamic lipid remodeling of the hepatic lipidome. J. Lipid Res. *65*, 100434. https://doi.org/10.1016/j.jlr.2023.100434.
41. Millar, J.S., Cromley, D.A., McCoy, M.G., Rader, D.J., and Billheimer, J.T. (2005). Determining hepatic triglyceride production in mice: comparison of poloxamer 407 with Triton WR-1339. J. Lipid Res. *46*, 2023–2028. https://doi.org/10.1194/jlr.D500019-JLR200.
42. Pan, Y., Li, Y., Gao, L., Tong, Z., Ye, B., Liu, S., Li, B., Chen, Y., Yang, Q., Meng, L., et al. (2017). Development of a novel model of hypertriglyceridemic acute pancreatitis in mice. Sci. Rep. *7*, 40799. https://doi.org/10.1038/srep40799.
43. Susulic, V.S., Frederich, R.C., Lawitts, J., Tozzo, E., Kahn, B.B., Harper, M.E., Himms-Hagen, J., Flier, J.S., and Lowell, B.B. (1995). Targeted disruption of the beta 3-adrenergic receptor gene. J. Biol. Chem. *270*, 29483–29492. https://doi.org/10.1074/jbc.270.49.29483.
44. Zhang, S., Hulver, M.W., McMillan, R.P., Cline, M.A., and Gilbert, E.R. (2014). The pivotal role of pyruvate dehydrogenase kinases in metabolic flexibility. Nutr. Metab. (Lond.) *11*, 10. https://doi.org/10.1186/1743-7075-11-10.
45. Nye, C.K., Hanson, R.W., and Kalhan, S.C. (2008). Glyceroneogenesis is the dominant pathway for triglyceride glycerol synthesis in vivo in the rat. J. Biol. Chem. *283*, 27565–27574. https://doi.org/10.1074/jbc.M804393200.
46. Kalhan, S.C., Mahajan, S., Burkett, E., Reshef, L., and Hanson, R.W. (2001). Glyceroneogenesis and the source of glycerol for hepatic triacylglycerol synthesis in humans. J. Biol. Chem. *276*, 12928–12931. https://doi.org/10.1074/jbc.M006186200.
47. Schäffer, L., Brand, C.L., Hansen, B.F., Ribel, U., Shaw, A.C., Slaaby, R., and Sturis, J. (2008). A novel high-affinity peptide antagonist to the insulin receptor. Biochem. Biophys. Res. Commun. *376*, 380–383. https://doi.org/10.1016/j.bbrc.2008.08.151.
48. Cheng, J.P.X., and Nichols, B.J. (2016). Caveolae: One Function or Many? Trends Cell Biol. *26*, 177–189. https://doi.org/10.1016/j.tcb.2015.10.010.
49. Parton, R.G., McMahon, K.A., and Wu, Y. (2020). Caveolae: Formation, dynamics, and function. Curr. Opin. Cell Biol. *65*, 8–16. https://doi.org/10.1016/j.ceb.2020.02.001.
50. Fernández, M.A., Albor, C., Ingelmo-Torres, M., Nixon, S.J., Ferguson, C., Kurzchalia, T., Tebar, F., Enrich, C., Parton, R.G., and Pol, A. (2006). Caveolin-1 is essential for liver regeneration. Science *313*, 1628–1632. https://doi.org/10.1126/science.1130773.
51. Ding, S.Y., Lee, M.J., Summer, R., Liu, L., Fried, S.K., and Pilch, P.F. (2014). Pleiotropic effects of cavin-1 deficiency on lipid metabolism. J. Biol. Chem. *289*, 8473–8483. https://doi.org/10.1074/jbc.M113.546242.
52. Fernández-Rojo, M.A., Restall, C., Ferguson, C., Martel, N., Martin, S., Bosch, M., Kassan, A., Leong, G.M., Martin, S.D., McGee, S.L., et al. (2012). Caveolin-1 orchestrates the balance between glucose and lipid-dependent energy metabolism: implications for liver regeneration. Hepatology *55*, 1574–1584. https://doi.org/10.1002/hep.24810.
53. Montagner, A., Polizzi, A., Fouché, E., Ducheix, S., Lippi, Y., Lasserre, F., Barquissau, V., Régnier, M., Lukowicz, C., Benhamed, F., et al. (2016). Liver PPARalpha is crucial for whole-body fatty acid homeostasis and is protective against NAFLD. Gut *65*, 1202–1214. https://doi.org/10.1136/gutjnl-2015-310798.
54. Dich, J., Hansen, S.E., and Thieden, H.I. (1973). Effect of albumin concentration and colloid osmotic pressure on albumin synthesis in the perfused rat liver. Acta Physiol. Scand. *89*, 352–358. https://doi.org/10.1111/j.1748-1716.1973.tb05530.x.
55. Chen, Q., Lu, M., Monks, B.R., and Birnbaum, M.J. (2016). Insulin Is Required to Maintain Albumin Expression by Inhibiting Forkhead Box O1 Protein. J. Biol. Chem. *291*, 2371–2378. https://doi.org/10.1074/jbc.M115.677351.
56. Kir, S., Beddow, S.A., Samuel, V.T., Miller, P., Previs, S.F., Suino-Powell, K., Xu, H.E., Shulman, G.I., Kliewer, S.A., and Mangelsdorf, D.J. (2011). FGF19 as a postprandial, insulin-independent activator of hepatic protein and glycogen synthesis. Science *331*, 1621–1624. https://doi.org/10.1126/science.1198363.
57. Najt, C.P., Adhikari, S., Heden, T.D., Cui, W., Gansemer, E.R., Rauckhorst, A.J., Markowski, T.W., Higgins, L., Kerr, E.W., Boyum, M.D., et al. (2023). Organelle interactions compartmentalize hepatic fatty acid trafficking and metabolism. Cell Rep. *42*, 112435. https://doi.org/10.1016/j.celrep.2023.112435.
58. Kang, S.W.S., Cunningham, R.P., Miller, C.B., Brown, L.A., Cultraro, C.M., Harned, A., Narayan, K., Hernandez, J., Jenkins, L.M., Lobanov, A., et al. (2024). A spatial map of hepatic mitochondria uncovers functional heterogeneity shaped by nutrient-sensing signaling. Nat. Commun. *15*, 1799. https://doi.org/10.1038/s41467-024-45751-9.
59. Rosenberger, F.A., Thielert, M., Strauss, M.T., Schweizer, L., Ammar, C., Mädler, S.C., Metousis, A., Skowronek, P., Wahle, M., Madden, K., et al. (2023). Spatial single-cell mass spectrometry defines zonation of the hepatocyte proteome. Nat. Methods *20*, 1530–1536. https://doi.org/10.1038/s41592-023-02007-6.
60. Droin, C., Kholtei, J.E., Bahar Halpern, K., Hurni, C., Rozenberg, M., Muvkadi, S., Itzkovitz, S., and Naef, F. (2021). Space-time logic of liver gene expression at sub-lobular scale. Nat. Metab. *3*, 43–58. https://doi.org/10.1038/s42255-020-00323-1.
61. Haas, J.T., Miao, J., Chanda, D., Wang, Y., Zhao, E., Haas, M.E., Hirschey, M., Vaitheesvaran, B., Farese, R.V., Jr., Kurland, I.J., et al. (2012). Hepatic insulin signaling is required for obesity-dependent expression of SREBP-1c mRNA but not for feeding-dependent expression. Cell Metab. *15*, 873–884. https://doi.org/10.1016/j.cmet.2012.05.002.
62. Abu-Elheiga, L., Matzuk, M.M., Abo-Hashema, K.A., and Wakil, S.J. (2001). Continuous fatty acid oxidation and reduced fat storage in mice lacking acetyl-CoA carboxylase 2. Science *291*, 2613–2616. https://doi.org/10.1126/science.1056843.
63. Patsch, W., Franz, S., and Schonfeld, G. (1983). Role of insulin in lipoprotein secretion by cultured rat hepatocytes. J. Clin. Invest. *71*, 1161–1174. https://doi.org/10.1172/jci110865.
64. Malmström, R., Packard, C.J., Caslake, M., Bedford, D., Stewart, P., Yki-Järvinen, H., Shepherd, J., and Taskinen, M.R. (1997). Defective regulation of triglyceride metabolism by insulin in the liver in NIDDM. Diabetologia *40*, 454–462. https://doi.org/10.1007/s001250050700.
65. Shvets, E., Bitsikas, V., Howard, G., Hansen, C.G., and Nichols, B.J. (2015). Dynamic caveolae exclude bulk membrane proteins and are required for sorting of excess glycosphingolipids. Nat. Commun. *6*, 6867. https://doi.org/10.1038/ncomms7867.
66. Cohen, A.W., Razani, B., Wang, X.B., Combs, T.P., Williams, T.M., Scherer, P.E., and Lisanti, M.P. (2003). Caveolin-1-deficient mice show insulin resistance and defective insulin receptor protein expression in adipose tissue. Am. J. Physiol. Cell Physiol. *285*, C222–C235. https://doi.org/10.1152/ajpcell.00006.2003.
67. Neuhaus, M., Fryklund, C., Taylor, H., Borreguero-Muñoz, A., Kopietz, F., Ardalani, H., Rogova, O., Stirrat, L., Bremner, S.K., Spégel, P., et al. (2023). EHD2 regulates plasma membrane integrity and downstream insulin receptor signaling events. Mol. Biol. Cell *34*, ar124. https://doi.org/10.1091/mbc.E23-03-0078.

68. Kim, J.A., Montagnani, M., Koh, K.K., and Quon, M.J. (2006). Reciprocal relationships between insulin resistance and endothelial dysfunction: molecular and pathophysiological mechanisms. Circulation *113*, 1888–1904. https://doi.org/10.1161/CIRCULATIONAHA.105.563213.

69. Suzuki, K., Hatzikotoulas, K., Southam, L., Taylor, H.J., Yin, X., Lorenz, K.M., Mandla, R., Huerta-Chagoya, A., Melloni, G.E.M., Kanoni, S., et al. (2024). Genetic drivers of heterogeneity in type 2 diabetes pathophysiology. Nature *627*, 347–357. https://doi.org/10.1038/s41586-024-07019-6.

70. Dobin, A., Davis, C.A., Schlesinger, F., Drenkow, J., Zaleski, C., Jha, S., Batut, P., Chaisson, M., and Gingeras, T.R. (2013). STAR: ultrafast universal RNA-seq aligner. Bioinformatics *29*, 15–21. https://doi.org/10.1093/bioinformatics/bts635.

71. Butler, A., Hoffman, P., Smibert, P., Papalexi, E., and Satija, R. (2018). Integrating single-cell transcriptomic data across different conditions, technologies, and species. Nat. Biotechnol. *36*, 411–420. https://doi.org/10.1038/nbt.4096.

72. Korsunsky, I., Millard, N., Fan, J., Slowikowski, K., Zhang, F., Wei, K., Baglaenko, Y., Brenner, M., Loh, P.R., and Raychaudhuri, S. (2019). Fast, sensitive and accurate integration of single-cell data with Harmony. Nat. Methods *16*, 1289–1296. https://doi.org/10.1038/s41592-019-0619-0.

73. Bankhead, P., Loughrey, M.B., Fernández, J.A., Dombrowski, Y., McArt, D.G., Dunne, P.D., McQuaid, S., Gray, R.T., Murray, L.J., Coleman, H.G., et al. (2017). QuPath: Open source software for digital pathology image analysis. Sci. Rep. *7*, 16878. https://doi.org/10.1038/s41598-017-17204-5.

74. Mina, A.I., LeClair, R.A., LeClair, K.B., Cohen, D.E., Lantier, L., and Banks, A.S. (2018). CalR: A Web-Based Analysis Tool for Indirect Calorimetry Experiments. Cell Metab. *28*, 656–666.e1. https://doi.org/10.1016/j.cmet.2018.06.019.

75. Liao, Y., Smyth, G.K., and Shi, W. (2014). featureCounts: an efficient general purpose program for assigning sequence reads to genomic features. Bioinformatics *30*, 923–930. https://doi.org/10.1093/bioinformatics/btt656.

76. Love, M.I., Huber, W., and Anders, S. (2014). Moderated estimation of fold change and dispersion for RNA-seq data with DESeq2. Genome Biol. *15*, 550. https://doi.org/10.1186/s13059-014-0550-8.

77. Young, M.D., and Behjati, S. (2020). SoupX removes ambient RNA contamination from droplet-based single-cell RNA sequencing data. GigaScience *9*, giaa151. https://doi.org/10.1093/gigascience/giaa151.

78. McGinnis, C.S., Murrow, L.M., and Gartner, Z.J. (2019). DoubletFinder: Doublet Detection in Single-Cell RNA Sequencing Data Using Artificial Nearest Neighbors. Cell Syst. *8*, 329–337.e4. https://doi.org/10.1016/j.cels.2019.03.003.

79. Dann, E., Henderson, N.C., Teichmann, S.A., Morgan, M.D., and Marioni, J.C. (2022). Differential abundance testing on single-cell data using k-nearest neighbor graphs. Nat. Biotechnol. *40*, 245–253. https://doi.org/10.1038/s41587-021-01033-z.

80. Kind, T., Liu, K.H., Lee, D.Y., DeFelice, B., Meissen, J.K., and Fiehn, O. (2013). LipidBlast in silico tandem mass spectrometry database for lipid identification. Nat. Methods *10*, 755–758. https://doi.org/10.1038/nmeth.2551.

81. Luan, H., Ji, F., Chen, Y., and Cai, Z. (2018). statTarget: A streamlined tool for signal drift correction and interpretations of quantitative mass spectrometry-based omics data. Anal. Chim. Acta *1036*, 66–72. https://doi.org/10.1016/j.aca.2018.08.002.

82. Chong, J., Wishart, D.S., and Xia, J. (2019). Using MetaboAnalyst 4.0 for Comprehensive and Integrative Metabolomics Data Analysis. Curr. Protoc. Bioinformatics *68*, e86. https://doi.org/10.1002/cpbi.86.

83. Demichev, V., Messner, C.B., Vernardis, S.I., Lilley, K.S., and Ralser, M. (2020). DIA-NN: neural networks and interference correction enable deep proteome coverage in high throughput. Nat. Methods *17*, 41–44. https://doi.org/10.1038/s41592-019-0638-x.

84. Stratton, K.G., Webb-Robertson, B.M., McCue, L.A., Stanfill, B., Claborne, D., Godinez, I., Johansen, T., Thompson, A.M., Burnum-Johnson, K.E., Waters, K.M., et al. (2019). pmartR: quality control and statistics for mass spectrometry-based biological data. J. Proteome Res. *18*, 1418–1425. https://doi.org/10.1021/acs.jproteome.8b00760.

85. Polpitiya, A.D., Qian, W.-J., Jaitly, N., Petyuk, V.A., Adkins, J.N., Camp, D.G., Anderson, G.A., and Smith, R.D.J.B. (2008). DAnTE: a statistical tool for quantitative analysis of-omics data. Bioinformatics *24*, 1556–1558. https://doi.org/10.1093/bioinformatics/btn217.

86. Webb-Robertson, B.J.M., Matzke, M.M., Jacobs, J.M., Pounds, J.G., and Waters, K.M.J.P. (2011). A statistical selection strategy for normalization procedures in LC-MS proteomics experiments through dataset-dependent ranking of normalization scaling factors. Proteomics *11*, 4736–4741. https://doi.org/10.1002/pmic.201100078.

STAR★METHODS

KEY RESOURCES TABLE

REAGENT or RESOURCE	SOURCE	IDENTIFIER
Antibodies		
Monoclonal Rat-anti-F4/80	Abcam	Cat: #ab6640; RRID:AB_1140040
Polyclonal Rabbit-anti-Rat	Abcam	Cat: #ab102248; RRID:AB_10711314
Polyclonal Rabbit-anti-GLUL	Thermo Fisher Scientific	Cat: #PA5-28940; RRID:AB_2546416
Polyclonal Rabbit-anti-HAL	Sigma-Aldrich	Cat: #HPA038547; RRID:AB_10669541
Monoclonal Rat-anti-PLVAP	BD Bioscience	Cat: #553849; RRID:AB_395086
Monoclonal Rabbit-anti-PDGFRa/b	Abcam	Cat: #32570; RRID:AB_777165
Polyclonal Rabbit-anti-DESMIN	Thermo Fisher Scientific	Cat: #RB-9014-P1; RRID: N/A
Polyclonal Goat-anti-DESMIN	R&D Systems	Cat: #AF3844; RRID:AB_2092419
Polyclonal Chicken-anti-mCherry	Abcam	Cat: #ab205402; RRID:AB_2722769
Polyclonal Rabbit-anti-PLIN2	Sigma-Aldrich	Cat: #HPA016607; RRID:AB_2669403
Polyclonal Goat-anti-CAV1	Abcam	Cat: #ab211503; RRID: N/A
Monoclonal Rabbit-anti-CAVIN1	Cell Signaling	Cat: #69036; RRID:AB_2799758
Polyclonal Rabbit-anti-Phospho-AKT (Ser473)	Cell Signaling	Cat: #9271S; RRID:AB_329825
Monoclonal Rabbit-anti-AKT	Cell Signaling	Cat: #4685S; RRID:AB_2225340
Monoclonal Rabbit-anti-PLVAP	Cell Signaling	Cat: #24764; RRID: N/A
Polyclonal Rabbit-anti-PDK4	Proteintech	Cat: #12949-1-AP; RRID:AB_2161499
Monoclonal Mouse-anti-TUBULIN	Sigma-Aldrich	Cat: #05-829; RRID:AB_310035
Polyclonal AlexaFluor®546 Donkey-anti-Goat	Thermo Fisher Scientific	Cat: #A11056; RRID:AB_2534103
Polyclonal AlexaFluor®568 Goat-anti-Chicken	Thermo Fisher Scientific	Cat: #A11041; RRID:AB_2534098
Polyclonal AlexaFluor®647 Donkey-anti-Rabbit	Jackson ImmunoResearch	Cat: #711-605-152; RRID:AB_2492288
STAR Red Goat-anti-Rabbit	Abberior	Cat: #STRED-1007; RRID: N/A
EnVision-HRP anti-Rabbit	Agilent	Cat: #K400311-2; RRID: N/A
Polyclonal HRP Goat-anti-Rabbit	Dako	Cat: #P0448; RRID:AB_2617138
Polyclonal HRP Goat-anti-Mouse	Dako	Cat: #P0447; RRID:AB_2617137
Chemicals, peptides, and recombinant proteins		
CL316,243	Sigma-Aldrich	Cat: #5976
S961 (InsR antagonist)	Novo Nordisk	#NNC0069-0961
Poloxamer-407	Sigma-Aldrich	Cat: #16758
Insulin	Novo Nordisk	#NNC0121-0308
Bovine Serum Albumin	Sigma-Aldrich	Cat: #A7030
HSC LipidTOX Green Neutral Lipid Stain	Thermo Fisher Scientific	Cat: #H34475
BODIPY FL C16 (Palmitic acid)	Thermo Fisher Scientific	Cat: #D3821
Taq Polymerase	Ampliqon	Cat: #A111107
Hematoxylin	Sigma-Aldrich	Cat: #MHS16
Eosin	Sigma-Aldrich	Cat: #HT110232
Citrate buffer (pH: 6.0)	Sigma-Aldrich	Cat: #C9999
Nuclei Extraction Buffer	Miltenyi Biotec	Cat: #130-128-024
2,4,6-Collidine Buffer	Thermo Fisher Scientific	Cat: #A11058.AP
Glutaraldehyde	Sigma-Aldrich	Cat: #1.12179.0025
Splash Lipidomix, Avanti Lipids	Sigma-Aldrich	Cat: #330707-1EA

(*Continued on next page*)

Continued

REAGENT or RESOURCE	SOURCE	IDENTIFIER
Immobilon Classico Western HRP Substrate	Millipore	Cat: #WBLUC0500
Critical commercial assays		
RNAscope Multiplex Fluorescent Reagent Kit V2	Advanced Cell Diagnostics	Cat: #323100
Monarch Total RNA Miniprep Kit	New England Biolabs	Cat: #T2010S
NEBNext Ultra RNA Library Prep Kit for Illumina	New England Biolabs	Cat: #E7770
Chromium Next GEM Single Cell 3′ GEM, Library and Gel Bead Kit version 3.1	10x Genomics	Cat: #PN-1000121
Pierce BCA Protein Assay Kit	Thermo Fisher Scientific	Cat: #23227
FUJIFILM NEFA HR(2) Kit	Wako Diagnostics	Cat: #434-91795 & #436-91995
Glycerol Assay Kit	Sigma-Aldrich	Cat: #MAK117-1KT
Ultra-sensitive Mouse Insulin ELISA Kit	Crystral Chem	Cat: #90080
FGF21 Quantikine ELISA	R&D Systems	Cat: #MF2100
Triglyceride Quantification Kit	Sigma-Aldrich	Cat: #MAK266
Deposited data		
Raw and processed sequencing data [GEO]	This Paper	GEO: GSE246088
Proteomics Data [ProteomeXchange]	This Paper	PRIDE: PXD046745
Data S1 – Source Data	This Paper	N/A
Public microarray data [GEO]	Fougerat et al.[29]	GEO: GSE165699
Public microarray data [GEO]	Régnier et al.[30]	GEO: GSE96559
Experimental models: Organisms/strains		
Mouse: C57BL/6JBomTac	Taconic	Cat: #B6JBOM-M
Mouse: C57BL/6NRj	Janvier	N/A
Mouse: Plvaptm1.1Salm (B6.126(Cg))	Rantakari et al.[21]	N/A
Mouse: Tg(Lrat-cre)1Rshw (B6;CBA)	Mederacke et al.[27]	N/A
Mouse: Gt(ROSA)26Sortm1(mCherry-Rpl10a-Flpo)Kra-Tg(Lrat-cre) 1Rshw (B6.Cg)	Bendixen et al.[28]	N/A
Mouse: Cav1tm1Mls/J	The Jackson Laboratory	JAX: #004585
Oligonucleotides		
Primer: Plvap, Forward: CGAGTCACCACAACGTACATG	This Paper	N/A
Primer: Plvap, Reverse: CGTCTGTAGTGGACAGTTCC	This Paper	N/A
Primer: Lrat-Cre, Forward: CGTACCGTACACCAAAATTTGCCTG	This Paper	N/A
Primer: Lrat-Cre, Reverse: CGGATCATCAGCTACACCAGAGAC	This Paper	N/A
Software and algorithms		
GraphPad Prism version 8.0	GraphPad Software	N/A
ImageJ	NIH	https://imagej.net
R	R Core Team	https://www.r-project.org
STAR version 2.7.8a	Dobin et al.[70]	https://github.com/alexdobin/STAR
Seurat version 4.9.9	Butler et al.[71]	https://satijalab.org/seurat/
Harmony version 0.1.1	Korsunsky et al.[72]	https://github.com/immunogenomics/harmony
NIS-Elements ER version 5.21.03 software	Nikon	N/A
QuPath version 0.2.3 software	Bankhead et al.[73]	https://qupath.github.io
CalR version 1.3	Mina et al.[74]	https://calrapp.org

(*Continued on next page*)

Continued

REAGENT or RESOURCE	SOURCE	IDENTIFIER
Other		
Chow Diet	Altromin	Cat: #1324
High-Fat Diet (HFD)	Research Diets	Cat: #D12492
Western Diet (WDF)	Special Diets Services	Cat: #829100
Freedom Lite Glucometer	Abbott Diabetes Care	N/A
GentleMACS Octo Dissociator	Miltenyi Biotec	Cat: #130-096-427
Fragment Analyser 5200	Agilent Technologies	Cat: #M5310AA
10x Genomics Chromium Controller	10x Genomics	Cat: #PN110203
FACSAria III (Fluorescence-Activated Cell Sorting)	Becton Dickinson	N/A
NovaSeq 6000	Illumina	N/A
TSE PhenoMaster NG 2.0	TSE Systems	N/A
Minispec LF50, benchtop TD-NMR	Bruker BioSpin	Cat: #E1400005-01
Nikon A1 Confocal Microscope	Nikon	N/A
Apreo S Field-Emission Scanning Electron Microscope	Thermo Fisher Scientific	N/A

Animal experiments

All transgenic mouse models used in this study are listed in the key resources table. Conditional male *Lrat-Cre*$^{wt/tg}$*:Plvap*$^{fl/fl}$ (*Plvap*$^{HSC\text{-}KO}$) mice, whole-body *Cav1* knockout mice, their respective controls, and *Lrat-Cre:FLEx-TRAP* reporter mice were housed under standard conditions at 22°C with a 12:12hr light/dark cycle and *ad libitum* access to chow (#1324, altromin) and drinking water unless otherwise specified. All animal experiments were approved by the Danish Animal Experiment Inspectorate (approval: 2020-15-0201-00603) or the Ethical Committee for Animal Experimentation in Finland (approval: #14685-2020) and adhered to ARRIVE guidelines. In all experiments we used age-matched male mice and used *Cre*-negative littermates as controls. In most experiments, the animals were 14-20 weeks of age. Some mice were fed a high-fat diet (#D12492, Research Diets) or a Western diet (#829100, Special Diets Services, Witham, UK) supplemented with D-fructose (42 g/L) in their drinking water for six weeks. Body weights was determined after 12-hour over-night (o.n.) fasting. To assess hepatic TAG-VLDL secretion, *Plvap*$^{HSC\text{-}KO}$ and *Plvap*$^{HSC\text{-}Flox}$ mice were fasted for 12h (20:00 to 08:00h, ZT14 to ZT2) to clear chylomicrons from circulation before inhibition of lipoprotein lipase by intraperitoneal (i.p.) injection with Poloxamer-407 (1g/kg, #16758, Sigma). After another hour of fasting, serum were obtained by centrifugation (4000g for 15 min. at 4°C) of whole blood. To study the role of insulin signaling, the insulin receptor antagonist S961 (500 nmol/kg; kind gift from Novo Nordisk A/S) or sterile 1x PBS were injected subcutaneously into 12h fasted animals two hours before sacrifice. Ad libitum fed mice were injected i.p. with CL316,243 (1mg/kg; #5976, Sigma-Aldrich) one hour before sacrifice to determine the effect of lipolysis in non-fasting animals. Blood glucose levels were assessed using a Freedom Lite glucometer (Abbott Diabetes Care Inc.) after 12h fasting. Indirect calorimetry was conducted at thermoneutrality (30°C) using a TSE PhenoMaster NG 2.0 (TSE Systems GmbH, Germany). Extended procedures are listed under method details.

METHOD DETAILS

Generation of conditional *Plvap*-deficient mice

For HSC-specific Plvap ablation, heterozygote *Plvap*-flox (*Plvap*^{tm1Salm}) mice[21] backcrossed to the C57BL/6JBomTac strain were bred with the *Lrat-Cre* line (Lrat-*Cre*^{1Rshw}) line[27] to obtain *Lrat-Cre*$^{wt/tg}$*-Plvap*$^{fl/fl}$ (*Plvap*$^{HSC\text{-}KO}$) mice. Genotyping was performed by PCR using *Plvap* forward 5′-CGAGTCACCACAACGTACATG-3′ and reverse 5′-CGTCTGTAGTGGACAGTTCC-3′ primers creating 350 and 210 bp PCR fragments for the *Plvap* floxed and wild type alleles, respectively. Likewise, the *Lrat-Cre* transgene was detected by primers; 5′-CGTACCGTACACCAAAATTTGCCTG-3′ and 5’-CGGATCATCAGCTACACCAGAGAC-3′ creating a 700 bp fragment in *Cre*-positive mice. Genomic DNA was obtained from tail tips or ear tissue and fragment sizes were determined by gel electrophoresis using a Fragment Analyzer 5200 (Agilent Technologies, Santa Clara, CA, USA) running a 35-1500 bp DNA marker (#FS-SMK910-0003, Agilent). PCR analysis was performed in 30 μl reaction volumes containing 1 μl mouse DNA, 21.08 μl milliQ-H_2O, 3 μl Taq Ammonium buffer (10x) (#A111107, Ampliqon), 0.72 μl dNTP (containing 10 mM of each), 1.8 μl forward and reverse primers (5 pmol/μl), and 0.6 μl Taq polymerase (#A111107, Ampliqon). Three-step PCRs were run under the following conditions: 1 cycle of 95°C for 2 min. followed by 35 cycles of 30 sec. at 95°C, 30 sec. at 60°C, 2 min. at 72°C, before 1 cycle of 72°C for 10 min.

Tissue and serum collection

Mice were either fasted 12 hours o.n. (20:00 to 08:00h, ZT14 to ZT2) or fasted and refed for two hours before euthanasia by cervical dislocation. Blood was obtained after decapitation, and organs collected for analyses. Serum was obtained by blood centrifugation at 4000g for 15 min. at 4°C. Liver tissues for RNA-sequencing were immediately snap-frozen using liquid nitrogen.

Ketone body measurements

Age-matched male *Plvap*$^{HSC-KO}$ and littermate control mice (n = 7) were fasted for 12 hours o.n. (20:00 to 08:00h, ZT14 to ZT2) or 24h with free access to water before measurement of β-hydroxybutyrate using a On-Call GK dual ketonemeter and matching ketone test strips (#GK134-90AA, Acon Laboratories, San Diego, CA).

Glucose (ipGTT) and insulin (ipITT) tolerance

Baseline blood glucose was measured in mice (n = 4-5) after 12h fasting and before i.p. injection of 2g/kg D-glucose in phosphate buffered saline (PBS). Blood glucose was then accessed using a Freedom Lite glucometer (Abbott Diabetes Care Inc.) 20 - 120 min. post injection. Likewise, a similar cohort of 12h fasted mice (n = 5-6) were injected with 1U/kg insulin in PBS (#NNC0121-0308, kind gift from Novo Nordisk A/S) and blood glucose was then assessed 20 - 180 min. post injection.

Immunohistochemical staining of FFPE tissues

Murine liver tissues were fixed in 4% paraformaldehyde (PFA) for 24 hours following paraffin-embedding (FFPE) and cut in 3 μm sections. Tissues were deparaffinized before hematoxylin and eosin staining (#MHS16 and #HT110232, Sigma-Aldrich, St. Louis, MO), Periodic acid–Schiff (PAS) or Picrosirius Red staining (Department of Pathology, OUH, Denmark). For immunohistochemistry of F4/80, HAL and GLUL, tissues were deparaffinized, and endogenous peroxidase was quenched using hydrogen peroxide (#R37629, Thermo Fisher Scientific, Waltham, MA) followed by heat-induced antigen-retrieval in citrate buffer, pH 6.0 (#C9999, Sigma-Aldrich). Sections were probed either with 1:1200 rabbit-anti-Glul (#PA5-28940, Thermo Fisher Scientific), 1:200 rabbit-anti-Hal (#HPA038547, Sigma), or 1:200 rat-anti-F4/80 (#ab6640, Abcam, Cambridge, UK) antibody followed by 1:200 rabbit-anti-rat IgG (#ab102248, Abcam). Sections were then added EnVision-HRP-coupled anti-rabbit IgG (#K400311-2, Agilent, Santa Clara, CA). For detection, AEC+ Substrate-Chromogen solution (#K346111-2, Agilent) or DAB+ Substrate-Chromogen solution (#K3467, Dako) was applied, and sections were counter-stained with hematoxylin (#MHS16, Sigma-Aldrich). Bluing of hematoxylin was performed using bluing buffer (#CS702, Dako). All staining's were visualized using an Olympus BX51 microscope running *cellSens* acquisition software.

Immunofluorescent confocal microscopy

For immunofluorescence, liver tissues were fixed in 4% PFA for four hours at 4°C and kept o.n. in a 20% sucrose solution. Tissues were O.C.T.-embedded (#361603E, VWR chemicals) and cut in 12 μm sections placed on *Superfrost plus* microscope slides (#J1840AMNZ, Thermo Fisher Scientific). Tissues were permeabilized for 30 min. in PBS with 0.3% Triton-X100 before adding blocking buffer containing 1% bovine serum albumin (BSA) (#81-066-40, Millipore) and 1% normal donkey serum (#017-000-121, Jackson ImmunoResearch) in PBS for 30 min. Tissues were probed with 1:100 primary antibody; rat-anti-PLVAP (#553849, BD Bioscience) alone or in combination with 1:25 goat-anti-Desmin (#AF3844, R&D Systems) o.n. at 4°C and washed in PBS before addition of 1:200 rabbit-anti-rat (#ab102248, Abcam) followed by 1:500 AlexaFluor546 donkey-anti-goat (#A11056, Thermo Fisher Scientific) and/or AlexaFluor647 donkey-anti-rabbit (#711-605-152, Jackson ImmunoResearch) and 1 μg/mL 4,6-diamidino-2-phenylindole (DAPI, #D9542, Sigma-Aldrich). For single detection of PDGFRα/β and Desmin, we used 1:100 rabbit-anti-PDGFRα/β (#32570, Abcam) or rabbit-anti-Desmin (#RB-9014-P1, Thermo Fisher Scientific) and 1:500 secondary antibody; AlexaFluor647 donkey-anti-rabbit (#711-605-152, Jackson ImmunoResearch). mCherry in livers of *Lrat-Cre:FLEx-TRAP* mice was boosted using 1:1000 chicken-anti-mCherry (#ab205402, Abcam) and 1:500 AlexaFluor568 goat-anti-chicken (#A11041, Thermo Fisher Scientific). Likewise, PLIN2 protein was detected using 1:100 rabbit-anti-PLIN2 (#HPA016607, Sigma) and 1:500 AlexaFluor647 donkey-anti-rabbit (#711-605-152, Jackson ImmunoResearch). Slides were mounted using Prolong Dimond Antifade Mountant (#P36961, Thermo Fisher Scientific) and visualized using a Nikon A1 confocal microscope running the NIS-Elements ER version 5.21.03 acquisition software.

Neutral lipid staining

Staining of neutral lipids was performed using HCS LipidTOX Green Neutral Lipid Stain (#H34475, Thermo Fisher Scientific). PFA-fixed, O.C.T. embedded liver, heart, kidney, and muscle tissues were cut at 12 μm and permeabilized in PBS with 0.3% Triton-X100 for 30 min. Slides were incubated for one hour at RT with 1:200 LipidTOX and DAPI (#D9542, Sigma-Aldrich), Wahsed in PBS and mounted using Prolong Dimond Antifade Mountant (#P36961, Thermo Fisher Scientific).

Fatty acid-BSA mouse i.v. injections

BODIPY-FL-C_{16} (#D3821, Thermo Fisher Scientific) was dissolved (500 μL; 1 mg/mL) in 100% ethanol. The solution was evaporated under nitrogen until 20 μl of concentrated lipid was left, and diluted in 30 μl 0.1 M NaOH before heating to 37°C and addition of 1035 μl BSA stock (6.65 mg/mL BSA (#A7030, Sigma) in 0.9% NaCl, 5 mM HEPES (#H0887, Sigma)). The solution was incubated for 15 min. at 37°C followed by brief sonication and stored dark at 4°C. Prior to use, the solution was re-heated to 37°C. 12 h-fasted mice were anesthetized (Avertin, #T48402, Sigma) and perfused (1 ml/min.) through the portal vein with wash buffer (1x PBS added 2 mM Glucose, 2 mM $CaCl_2$ and 5 mM HEPES (#H0887, Sigma). After perfusion start, 100 μl 0.5 mM BODIPY-FL-C_{16} - BSA complex was infused followed by 4 ml wash buffer and 10 ml 4% PFA. After dissection, livers were fixed in 4% fresh PFA for 4 hours at

4°C and embedded in O.C.T. Tissue sections (12 μm) were permeabilized for 15 min. in PBS with 0.3% Triton-X100 and counterstained with DAPI for visualization on a Nikon A1 confocal microscope running the NIS-Elements ER version 5.21.03 acquisition software.

RNA fluorescent *in situ* hybridization

RNA fluorescent *in situ* hybridization was performed using the *RNAscope* Multiplex Fluorescent Reagent Kit v2 (#323100, Advanced Cell Diagnostics, Newark, CA). In brief, FFPE sections were deparaffinated and blocked in hydrogen peroxide (#322381, ACD) before boiling in target retrieval reagent (#322000, ACD) for 30 min. Sections were incubated with RNAscope protease plus (#322381, ACD) for 40 min. and hybridized with mm-Plvap (#440221, ACD), mm-Lrat (#460641, ACD) and mm-Stab2 (#406611, ACD) probes for two hours at 40°C. Probes were detected with Opal 570 (1:1000, #OP-001003, Akoya Biosciences), Opal 690 (1:1000, #OP-001006, Akoya Biosciences, Marlborough, USA), and Opal 520 (1:750, #OP-001001, Akoya Biosciences) fluorescent dyes, respectively, and counterstaining with DAPI (#323108, ACD). Slides were mounted using Prolong Diamond Antifade Mountant (#P36961, Thermo Fisher Scientific) and imaged using a Nikon confocal A1 microscope running the NIS-Elements ER version 5.21.03 acquisition software.

Histological quantifications

Digital quantifications of Immunofluorescent images were performed using QuPath v.0.2.3.[73] Positive staining was detected using random forest pixel classification with *very high* (0.41 μm/px) resolution and used to calculate the fluorescent positive area relative to the entire area.

RNA purification, sequencing, and data analysis

Snap-frozen, pulverized liver tissue was homogenized using FastPrep-24 (MP biomedicals, Irvine, CA), and whole RNA was extracted using the Monarch Total RNA Miniprep Kit (NEB #T2010S, New England BioLabs). RNA concentrations were measured on a Qubit 3.0 Fluorometer (Thermo Fisher Scientific), and RNA integrity determined using a Fragment Analyzer 5200 (Agilent, Santa Clara, CA). Sequencing libraries were prepared with the NEBNext Ultra RNA Library Prep Kit for Illumina (#E7770, New England Biolabs, San Diego, CA) and paired-end sequenced on a NovaSeq™ 6000 Illumina instrument. Reads were aligned to the GRCm39 v.101 mouse genome using STAR v.2.7.8a[70] and processed by featureCounts v.2.0[75] for exon read counting. Counts were normalized for data analysis using variance stabilised transformation. Differentially expressed genes (DEGs) were determined using DESeq2.[76] For differential expression, adjusted p-values < 0.05 were considered statistically significant.

Nuclei isolation and snRNAseq

Nuclei from 30 mg fresh-frozen liver tissue were extracted in 1 ml nuclei extraction buffer (#130-128-024, Miltenyi Biotec, Germany) and 0.5 U/μl Protector RNase inhibitor (#04897030001, Roche, Germany) in C-tubes (#130096334, Miltenyi Biotec) by disruption on a GentleMACS Octo dissociator running the 4C-nuclei-1 program. Tissue suspensions were filtered through a 70 μm Smartstrainer (#130-110-916, Miltenyi Biotec) and diluted to 5 mL in 3 mL nuclei suspension buffer (NSB, 25 mM Tris-HCl pH 7.5, 2.5 mM $MgCl_2$, 16.7 mM KCl, 500 mM sucrose, 0.8 mM spermidine, 0.2 U/μL RNase inhibitor, and 1% BSA in DEPC-H_2O) and 1 ml 1% BSA in DEPC-H_2O. Samples were then centrifuged at 300g for 5 min. at 4°C, supernatants removed, and pellets resuspended in 300 μl NSB without sucrose and spermidine. The nuclei were then filtered through a 40 μm tip strainer (#H13680-0040, Flowmi, Sigma-Aldrich, St. Louis, MO, USA) and stained with 5 μM DRAQ5 DNA dye (#62254, Thermo Fisher Scientific) before fluorescence-activated nuclear sorting. DRAQ5$^+$ nuclei were identified and sorted as singlets on a FACSAria™ III with a 100 μm nozzle (Becton Dickinson (BD) Biosciences, Franklin Lakes, NJ) using the BD FACSDiva™ software v.8.0.1. 10000 DRAQ5$^+$ nuclei per sample were immediately loaded onto a Chromium controller (10x Genomics). Libraries were constructed using the Chromium Next GEM Single Cell 3′ GEM, Library and Gel Bead kit v.3.1 (PN-1000121, 10x Genomics). cDNA libraries were sequenced using the Illumina NovaSeq™ 6000 instrument.

SnRNAseq data analysis

Sequencing data was aligned to the mm10 reference genome and quantified using the Cell Ranger Single Cell Software Suite (ver. 7.1.0). We employed SoupX (ver. 1.6.2) to estimate and remove nuclei-free ambient RNA in droplets.[77] The Seurat package (ver. 4.9.9) was used to pre-process the data.[71] Low-quality nuclei with < 200 features, a mitochondrial gene contribution > 2%, or with < 200 or > 5000 total counts were removed. Genes expressed in less than 50 nuclei were removed. Doublets were detected and removed using the R package DoubletFinder (ver. 2.0.3).[78] Counts were normalized and log1p-transformed using Seurat SCTransform. We captured 1.47 billion reads with an average of 54713 reads per nucleus. After pre-processing and clean-up, 22609 single nuclei remained. Samples were integrated using Harmony (ver. 0.1.1)[72] and uniform manifold approximation and projection (UMAP) was performed in Seurat. For clustering, we used the Seurat implementation of the Louvain algorithm. Resolution parameters were set to obtain clusters displaying the most biological meaning and variability. Differential gene expression analysis was performed using the Wilcoxon rank-sum test. We performed a differential abundance analysis using the miloR package.[79] The k-nearest neighbor (knn) graph was computed based on the batch corrected embeddings computed as described previously using Harmony.[72] For the knn construction the number of nearest neighbors was set to 50. The nhood abundance testing was set to a significance level of 0.1. All data visualization and statistics was performed in R.

Total serum protein measurements

The total protein concentrations in serum samples were determined using the Pierce™ BCA protein assay kit (#23227, Thermo Fisher Scientific). In short, 0.5 μL serum was mixed in 24.5 μL H_2O and added BCA reagent followed by incubation for 20 min. Absorbance was measured at 562 nm using a CLARIOstar instrument (BMG Labtech) running version 5.40 R3 acquisition software. Protein concentrations were calculated based on a BSA standard curve.

Serum NEFA and glycerol measurements

Serum non-esterified fatty acids (NEFA) were quantified using the Fujifilm NEFA-HR(2) kit (#434-91795 & #436-91995, Wako Diagnostics) and a standard curve of NEFA standards (#270-77000, Wako Diagnostics). The colorimetric absorbance was measured at 550 nm. Serum glycerol was quantified using the Glycerol Assay Kit (#MAK117-1KT, Sigma). Glycerol concentrations were determined by colorimetric absorbance at 570 nm using a CLARIOstar instrument (BMG Labtech) running version 5.40 R3 acquisition software.

ELISAs

For measurement of serum insulin after 12h fasting or 2h refeeding, we used the Ultra-sensitive Mouse Insulin ELISA kit (#90080, Crystal Chem). Serum FGF-21 levels after fasting were determined using the Quantikine ELISA (#MF2100, R&D Systems).

Triglyceride measurements

Serum TAGs were determined using the Triglyceride Quantification Kit (#MAK266, Sigma) and a CLARIOstar plate reader (BMG Labtech) for colorimetric measurements at 570 nm.

Stimulated emission depletion microscopy

For combined stimulated emission depletion (STED) and confocal microscopy, PFA-fixed, cryo-preserved (O.C.T.) liver tissues were cut in 10 μm sections. Antibody labeling of PLVAP (1:100, #553849, BD Bioscience) together with mCherry (1:1000, #ab205402, Abcam) protein was performed as described for confocal microscopy but using STAR RED goat-anti-rabbit (1:250, #STRED-1007, Abberior, Göttingen, Germany) for PLVAP detection. For combined PLVAP and CAV1 detection, we used rat-anti-PLVAP (1:100, #553849, BD Bioscience) and goat-anti-CAV1 (1:50, #ab211503, Abcam) primary antibodies. For PLVAP detection, we used the linker antibody rabbit-anti-rat (1:200, #ab102248, Abcam) and STAR RED goat-anti-rabbit (1:250, #STRED-1007, Abberior). We detected CAV1 with AlexaFluor546 donkey-anti-goat (1:500, #A11056, Thermo Fisher Scientific). For dual CAV1 and CAVIN1 detection, we used goat-anti-Cav1 (1:50, #ab211503, Abcam) and rabbit-anti-Cavin1 (1:300, #69036, Cell Signaling) antibodies, followed by AlexaFluor546 donkey-anti-goat (1:500, #A11056, Thermo Fisher Scientific) and STAR RED goat-anti-rabbit (1:250, #STRED-1007, Abberior). All slides were mounted with Prolong Diamond Antifade Mountant (#P36961, Thermo Fisher Scientific). STED microscopy was performed on a Abberior Facility Line STED on an Olympus IX83 microscope with a 100x objective, running the iMSPECTOR version 16.3.13787 acquisition software. We applied a mean filter with a radius of one pixel to remove background noise.

Scanning and transmission electron microscopy

Male *Plvap*$^{HSC\text{-}KO}$ and littermate control mice were i.p. injected with 100 U heparin in PBS. After 5 min., the mice were anesthetized, surgically opened by laparotomy, and cardiac perfused using prewarmed 37°C RPMI1640 (#11879-020, Gibco) and PBS (1:1) at 5 mL/min for 5 min. Mice were then perfusion-fixed for 10 min. with 37°C fixative containing 2% glutaraldehyde (#1.12179.0025, Sigma) and 4% PFA in 0.2 M 2,4,6-collidine buffer (#A11058.AP, Thermo Fisher Scientific). Liver tissues were excised, cut into 1 x 1 x 4 mm. pieces, and submerged in new fixative at RT for 45 min. before rinse in 0.1 M sodium phosphate buffer. For transmission electron microscopy post-fixation, tissues were incubated in 2% OsO_4 containing 3% potassium ferrocyanide at room temperature for 2 hours. Samples were then dehydrated with a series of increasing ethanol concentrations (70%, 96%, and twice 100%) and embedded using an Epoxy Embedding Medium kit (#45359, Fluka). The samples were then trimmed and an ultramicrotome (Leica EM UC7) was used to cut 70 nm sections. The sections were subsequently stained with 1% uranyl acetate and 0.3% lead citrate and examined with a JEM-1400 Plus transmission electron microscope (JEOL ltd., Tokyo, JP). For scanning electron microscopy tissues were post-fixed as described above for TEM and dehydrated with a series of increasing ethanol concentrations (30%, 50%, 70%, 80%, 90%, 96% and twice 100%). Samples were frozen by immersion in liquid nitrogen and subjected to manual fracturing under liquid nitrogen. Fractured tissues were immersed in 100% hexamethyldisilazane and left to dry by solvent evaporation. The dried pieces were placed on aluminum stubs using adhesive carbon tabs and sputter coated with 5 nm of platinum (Quorum Q150V, Quorum Technologies Ltd, UK). The samples were analyzed using an Apreo S field-emission scanning electron microscope (Thermo Fisher Scientific) operating at 2 kV accelerating voltage.

Lipidomics mass-spectrometry

Lipids were extracted from 30 mg snap-frozen, non-perfused liver tissue by adding 1000 μl ice-cold solvent as a mixture of (1:2) methanol (#0013684101BS, Biosolve B.V., Valkenswaard, NL) and chloroform (#1.02444.2500, Sigma) containing internal standards (6 μL each/sample, Splash Lipidomix, Avanti Lipids (#330707-1EA, Sigma)). Samples were added 200 μL ULC/MS grade H_2O before shaking for 30 min. at 1000 rpm, 4°C. Samples were homogenized by sonication for 15 min. (8 cycles of 30 sec.) and centrifuged

for 10 min. at 16000g, 4°C. Aqueous and organic phases were separated, and the aqueous phase was reextracted with 350 μL cold chloroform/methanol/water (86/14/1) shaking for 20 min. at 1000 rpm, 4°C, and centrifugation for 10 min. at 16000g at 4°C. Organic phases were pooled and dried under a stream of nitrogen, and samples kept at -20°C until analysis. For lipidomics, dried samples were resuspended in 25 μL (1:1) methanol/chloroform, shaking for 5 min. at 1400 rpm, RT, followed by centrifugation for 5 min. at 16000g, RT. As quality control, 5 μL from each sample were mixed and analyzed by mass spectrometry to evaluate data reliability and for use for sample normalization. The remaining 20 μL of each sample were analyzed individually. Samples (0.5 μl) were injected using a Vanquish Horizon UPLC (Thermo Fisher Scientific) equipped with a Waters ACQUITY Premier CSH (2.1 x 100mm, 1.7 μM) column operated at 55°C.

The Lipidomics analytes were eluted using a flow rate of 400 μL/min. and the following composition of eluent A (Acetonitrile/water (60:40), 10 mM ammonium formate, 0.1% formic acid) and eluent B (Isopropanol/acetonitrile (90:10), 10 mM ammonium formate, 0.1% formic acid): 40% B from 0 to 0.5 min., 40–43% B from 0.5 to 0.7 min., 43-65% B from 0.7 to 0.8 min., 65-70% B from 0.8 to 2.3 min., 70-99% B from 2.3 to 6 min., 99% B from 6-6.8 min., 99-40% B from 6.8-7 min. before equilibration for 3 min. with the initial conditions. The flow from the UPLC was coupled to a TimsTOF Flex instrument (Bruker, Billerica, US) for mass spectrometric analysis, operated in both positive and negative ion modes using trapped ion mobility spectrometry. Data was processed in Metaboscape (v.2022, Bruker). Annotation was done using both an inbuild rule-based annotation approach and the LipidBlast MS2 library.[80] Features were removed if their average signal were not > 5x more abundant in the QC samples than blanks (water extraction). Signals were normalized to internal standards in the SPLASH mix before correction for signal drift using statTarget.[81] Finally, signals were normalized using the QC samples, before $\log_{10}$ transformation and auto scaling in Metaboanalyst.[82] Absolute values of DAGs and TAGs were estimated by normalizing to the known quantity of the respective lipid class representative present in internal standards.

LC-MS/MS proteomics and analysis

Serum proteins (100 μg) were reduced with 2 mM dithiothreitol at RT for 45 min., alkylated with 11 mM iodoacetamide at RT for 60 min., then digested with Lys-C for two hours and added 1 μg of modified trypsin (Promega, Madison, USA) for 18 hours at 37°C. After digestion, samples were acidified to 0.1% trifluoracetic acid (TFA), final concentration, and desalted on microcolumn StageTips made from P200 pipette tips plugged with two C18 discs. Peptide concentrations were measured using a nanodrop and ~1 μg of each digested sample was applied into an analytical column (New Objective x 75 μm internal diameter x 1.9 μm particle size ReproSil-Pur 120 C18-AQ, DR. MAISCH) heated to 50°C using a column heater. Separation of samples by liquid chromatography (LC) prior to injection into the mass spectrometer was conducted using an Easy-nLC 1200 system (Thermo Fisher Scientific) coupled to an Exploris 480 mass spectrometry (Thermo Fisher Scientific). Data were obtained using Xcalibur software (version 4.4.16.14). For data analysis, correlations between conditions were calculated after removal of all missing values and Pearson correlation coefficients were applied to check statistical differences. Peptide data was searched using DIA-NN[83] against a FASTA file downloaded from UniProt in September 2022. The parameters used for the search included carbamidomethylation of cysteines as a fixed modification and the variable modifications methionine oxidation and N-terminal acetylation. Trypsin was used as the digestive enzyme, missed cleavages were set to a maximum of two and default false discovery rate (FDR < 0.01). The main search peptide tolerance was set to 10 ppm. The data was analyzed with the pmartR package in R[84] for quality control and statistical analysis and then $\log_2$- transformed. Peptides matching more than one protein, peptides with less than 75% quantitation across samples, and peptides not susceptible to ANOVA or g-test were excluded. Protein rollup was performed with the DAnTE tool[85] in pmartR with default parameters. Comparisons subjected to the independence of missing data and ANOVA were submitted to robust Mahalanobis distance analysis for outlier diagnosis, based on median absolute deviation, asymmetry, correlation, and proportion of missing values. The abundance data were normalized according to the SPANS tool[86] present in pmartR.

Indirect calorimetry analysis

Metabolism was assessed in male *Plvap*$^{HSC\text{-}KO}$ and littermate control mice in a TSE PhenoMaster NG 2.0 (TSE Systems GmbH) after seven days of acclimatization. Mice were individually housed at thermoneutrality (30°C) with a 12/12-hour light/dark cycle and fed standard chow (#1324, altromin). We recorded gas exchange (VO_2 and VCO_2), food intake and animal activity every minute during the experiment. We subjected the mice to 24 hours of fasting (beginning 20:00h, ZT14) and re-feeding. Respiratory exchange ratio (RER) was calculated as VCO_2/VO_2. Statistical analysis, calculations and visualization of calorimetry data was performed with the tool CalR (version 1.3).[74]

NMR scanning for body composition analysis

To determine body compositions of male *Plvap*$^{HSC\text{-}KO}$ and littermate control mice, we fasted the mice for 12 hours o.n. (from 20:00 to 08:00h) and subjected each mouse to Minispec Time Domain NMR scanning analysis (Minispec LF50, benchtop TD-NMR, Bruker BioSpin GmbH, Germany) to resolve lean mass, fat mass, and free body fluid in live mice.

Western blot analysis

For western blotting, tissue lysates were prepared from frozen liver, kidney, muscle, and intestine using a Triton-X100 lysis buffer (1% Triton-X100, 150 mM NaCl, 50 mM Tris-HCl, and 2 mM EDTA) wth protease inhibitors (cOmplete and 1 mM Phenylmethylsulfonyl fluoride) and phosphatase inhibitors (25 mM Sodium Fluoride, 10 mM Sodium Pyrophosphate, 30 mM β-glycerolphosphate, and

1 mM Sodium Orthovanadate). Protein concentrations were quantified using the Pierce BCA protein assay kit (#23227, Thermo Fisher Scientific). Proteins were boiled in SDS loading buffer (50 mM Tris-HCl (pH: 6.8), 2% SDS, 6% glycerol, 1% β-mercaptoethanol, 0.004% bromophenol blue), resolved by SDS gel electrophoresis on 10% acrylamide gels, and transferred to PVDF membranes (#10600021, GE Healthcare Life science). Membranes blocked using 5% non-fat dry milk or 5% BSA in TBS and probed with anti p-AKT (Ser473) (#9271S, Cell Signaling), AKT (#4685S, Cell Signaling), PLVAP (#24764, Cell Signaling), PDK4 (#12949-1-AP, Proteintech), or Tubulin (#05-829, Sigma) over-night at 4°C. PVDF membrane washes was performed using TBS added 0.1% Tween-20 (TBST). HRP-conjugated secondary antibodies goat-anti-rabbit (#P0448, Dako) or goat-anti-mouse (#P0447, Dako) were diluted in 5% milk and added for one hour at RT. Immobilon Classico Western HRP Substrate (#WBLUC0500, Millipore) was used for detection on an Amersham Imager 680 instrument (GE Healthcare Bio-sciences Corp.).

QUANTIFICATION AND STATISTICAL ANALYSIS

Details on statistical tests are available in figure legends where applicable. Each [n] represents individual animals in each statistical group. Statistical analysis was performed between two groups using unpaired two-tailed Welch's or Student's t-test using GraphPad Prism version 8.0 (GraphPad Software, La Jolla, California, USA). Data in boxplots are represented as medians, upper and lower quartiles with whiskers showing maximum and minimum values, otherwise as mean ± SEM. For all analyses, group differences with $p < 0.05$ (where applicable adjusted for multiple testing) were considered statistically significant. For snRNAseq, data exclusion was driven by quality filtering (as described above) and data stratification was performed by Louvain clustering. For statistics of acute, indirect calorimetry, we used CalR (version 1.3)[74] to visualize data and conduct ANOVA for the study of RER differences. For lipidomics analyses we applied a t-test with Benjamini-Hochberg correction to adjust for type-I error accumulation (multiple testing) and considered lipids with an adjusted p-value < 0.05 to be statistically significant. Significance indicators: *$p < 0.05$, **$p < 0.01$, ***$p < 0.001$, ****$p < 0.0001$.